Opto-Electronic Technology

CN 51-1811/O4 ISSN (Print) 2097-6003 ISSN (Online) 2097-8006

Multi-dimensional photodetection: from material intrinsic properties and metasurface engineering to silicon photonic integration

Wenqi Liu, Zilan Tang, Qingzhao Hua, Liang Liu, Xiaoxia Wang* and Anlian Pan*

Citation: Liu WQ, Tang ZL, Hua QZ, et al. Multi-dimensional photodetection: from material intrinsic properties and metasurface engineering to silicon photonic integration. *Opto-Electron Technol* **2**, 260001 (2026).

https://doi.org/10.29026/oet.2026.260001

Received: 2 January 2026; Accepted: 13 February 2026; Published online: 19 March 2026

Related articles

Thin-film lithium niobate-based detector: recent advances and perspectives

Xiaoli Sun, Yuechen Jia, Feng Chen

Opto-Electronic Science 2025, **4**(12): 250028 doi: 10.29026/oes.2025.250028

Integrated photonic polarizers with 2D reduced graphene oxide

Junkai Hu, Jiayang Wu, Di Jin, et al

Opto-Electronic Science 2025, **4**(5): 240032 doi: 10.29026/oes.2025.240032

Highly enhanced UV absorption and light emission of monolayer WS_2 through hybridization with Ti_2N MXene quantum dots and g-C_3N_4 quantum dots

Anir S. Sharbirin, Rebekah E. Kong, Wendy B. Mato, et al

Opto-Electronic Advances 2024, **7**(6): 240029 doi: 10.29026/oea.2024.240029

Progress in metalenses: from single to array

Chang Peng, Jin Yao, Din Ping Tsai

Opto-Electronic Technology 2025, **1**(1): 250004 doi: 10.29026/oet.2025.250004

More related articles in Opto-Electronic Journals Group website

OET Opto-Electronic Technology

Review

March 2026, Vol. 2, No. 1

Open Access

Multi-dimensional photodetection: from material intrinsic properties and metasurface engineering to silicon photonic integration

Wenqi Liu[1], Zilan Tang[1], Qingzhao Hua[1], Liang Liu[1], Xiaoxia Wang[1]* and Anlian Pan[1,2]*

Abstract: Integrated photodetectors capable of decoding multi-dimensional optical information are essential for modern information technologies and are widely applicable in areas such as autonomous driving, optical communications, and remote sensing. Recent progress in this field has been driven by the synergy among advances in low-dimensional materials, micro/nanofabrication technologies, and computational algorithms, which have enabled notable developments in integrable multidimensional optical-field detectors. In this review, we first introduce some basic principles of multi-dimensional light detection and outline the critical strategies for frontend optical encoding and backend computational decoding. Subsequently, we discuss detection schemes based on the intrinsic optical properties of low-dimensional materials. We then move to metasurface architectures that use subwavelength structural engineering to enable multi-dimensional light field detection. Furthermore, we summarize recent research on silicon-photonic integrated multidimensional photodetection that combines sensing and computing units. To conclude, we summarize key challenges, such as wafer-scale synthesis and interface engineering, and envision a future in which photodetectors evolve from simple signal converters into programmable, intelligent systems capable of comprehensive light-field perception.

Keywords: multidimensional photodetection; 2D materials; metasurfaces; silicon photonics; light field manipulation; multidimensional light field

DOI: 10.29026/oet.2026.260001 | CSTR: 32419.14.oet.2026.260001

Citation: Liu WQ, Tang ZL, Hua QZ et al. Multi-dimensional photodetection: from material intrinsic properties and metasurface engineering to silicon photonic integration. *Opto-Electron Technol* **2**, 260001 (2026).

1 Introduction

Photodetectors serve as fundamental components in modern information technologies, with extensive applications in communications, imaging, medical diagnostics, military systems, and environmental monitoring[1–5]. Conventional photodetectors are primarily designed to convert optical intensity into electrical signals[6–9]. However, light propagating in free space carries multiple degrees of freedom, such as wavelength, polarization, and optical angular momentum[10–12]. Together, these independent or coupled physical dimensions constitute a high-dimensional space of light that contains rich information beyond what traditional intensity detection can access[13–15]. The development of photodetectors capable of simultaneously resolving multiple optical degrees of freedom within a single device holds great potential to enhance the information capacity and detection accuracy of optical systems[16,17]. This is crucial for high-dimensional information encoding and fine perception in national defense, security monitoring, remote sensing imaging, and quantum information[18–22].

Despite the broad application prospects of multidimensional photodetection, realizing this goal in monolithic integrated devices remains a significant challenge. First, an inherent physical coupling exists among the different physical dimensions of the optical field during photoelectric conversion. For instance, it is difficult to decouple polarization and wavelength fully. Concurrently, device design necessitates trade-offs among responsivity, dynamic range, and response speed[23–25]. Second, traditional detection

Received: 2 January 2026
Accepted: 13 February 2026
Published online: 19 March 2026

[1]Hunan Institute of Optoelectronic Integration and Key Laboratory for MicroNano Physics and Technology of Hunan Province, State Key Laboratory of Chemo/Biosensing and Chemometrics, College of Materials Science and Engineering, Hunan University, Changsha 410082, China; [2]School of Physics and Electronics, Hunan Normal University, Changsha 410081, China.
*Correspondence: XX Wang, E-mail: wangxiaoxia@hnu.edu.cn; AL Pan, E-mail: Anlian.Pan@hnu.edu.cn

methods often rely on bulky discrete optical components, which makes it challenging to meet the miniaturization requirements for on-chip integration[26–30]. Furthermore, multiplexed electrical outputs must be compatible with current electronic or photonic readout architectures and must be free of mutual hardware-level interference[31]. This imposes strict constraints on material selection, device design, and signal decoding algorithms. Therefore, the development of detection architectures capable of concurrently resolving multiple optical dimensions on a single chip has emerged as a critical direction in contemporary optoelectronics and intelligent photonic information processing.

With atomic thickness, pristine interfaces, and tunable propecc offer a versatile platform for multidimensional photodetection[32–38]. For instance, graphene enables broadband, high-speed sensing[39–42], transition metal dichalcogenides (TMDs) facilitate spectral discrimination[43–45], and anisotropic materials like ReS_2, $ReSe_2$, black phosphorus (BP) enable polarization detection[46–49]. Furthermore, complementary technologies such as artificial metasurfaces and photonic integration are being actively explored to expand detection dimensions, paving the way for advanced optical sensing systems[50–53]. Recent reviews have summarized advancements in photodetection from various perspectives[54,55]. Zhang et al. examined the optimization of 2D infrared detectors[56], while Yang et al. reviewed polarization-sensitive perovskite devices[57]. Furthermore, Zhao et al. highlighted the enhanced sensitivity and speed of metasurface photodetectors[58], and Xin et al. detailed the architectures of low-dimensional materials for polarized imaging[59]. Despite this progress, existing reviews primarily focuses on the detection individual optical degrees of freedom. There is a critical need for a review that comprehensively summarizes the development of integrated systems capable of resolving multiple optical dimensions and their advancement toward silicon photonic integration.

To explicitly delineate the scope of this review, we define multidimensional photodetectors as chip-scale optoelectronic perception architectures capable of resolving high-dimensional optical information. Distinct from traditional discrete instrumentation, these systems use microstructured optical elements to perform sophisticated light-field encoding. Regardless of whether they are implemented as single-pixel or multi-component microsystems, they share a unified goal: to achieve comprehensive light-field perception within a compact, integrable form factor by co-optimizing optical modulation hardware and computational reconstruction software. This evolution from discrete optical setups to all-integrated intelligent architectures is a hallmark of the next-generation photodetectors reviewed herein.

Guided by this comprehensive framework, this review summarizes the development of multidimensional photodetectors that directly decode multiple optical degrees of freedom on a single chip, as schematically illustrated in Fig. 1.

This review is structured into four main sections to provide a systematic overview of multidimensional photodetection. The first section introduces fundamental optical degrees of freedom and the physical principles governing their detection. Building on this, the next section establishes the theoretical basis, modeling sensing as a linear inverse problem and defining strategies for frontend encoding and backend decoding. The following section examines key advances in multidimensional detection enabled by intrinsic anisotropy of low-dimensional materials, tailored metasurfaces, and other photonic integration platforms. The final part discusses readout circuitry, signal processing methods, and persistent technical challenges in the field. By bridging fundamental mechanisms with device-level implementation, this review aims to establish a comprehensive framework for multidimensional photodetection that not only provides practical guidance for designing high-performance integrated photodetection systems but also clarifies future development trends in this field.

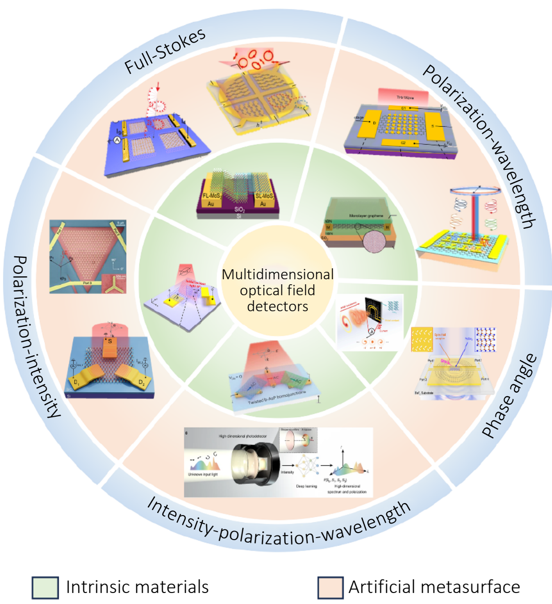

Fig. 1 | Multi-dimensional optical field photodetectors.

2 Physical dimensions of light fields

Light, as an electromagnetic wave, is characterized by its electric field distribution. Under the framework of classical electromagnetism, the electric field of a monochromatic beam is generally written as

$$\boldsymbol{E}\left(r,\phi,z,t\right)=E_0 f\left(r\right)\mathrm{e}^{\mathrm{i}\ell\phi}\widehat{\boldsymbol{e}}\cos\left(kz-\omega t\right)\ , \tag{1}$$

where $E\left(r,\ \phi,\ z,\ t\right)$ is the electric field as a function of radial distance r, azimuthal angle ϕ, propagation distance z, and time t. E_0 is the field amplitude, $f(r)$ describes the transverse profile of the beam, $\hat{\boldsymbol{e}}$ denotes the polarization vector, and $e^{i\ell\phi}$ represents the helical phase associated with orbital angular momentum (OAM), with ℓ being the topological charge that determines the phase winding around the axis. The term $\cos(kz-\omega t)$ describes the propagation of the wave along the z-direction and its oscillation in time, where k and ω correspond to the wave number and angular frequency, respectively. This compact expression incorporates the key physical quantities of light, including intensity, wavelength, polarization, and OAM, which constitute the fundamental information dimensions in modern optoelectronic systems, as summarized in Fig. 2.

2.1 Optical intensity

Optical intensity represents the energy density of the beam. In classical electromagnetism, the intensity is proportional to the square of the field amplitude and can be written as

$$I=\frac{1}{2}c\varepsilon_0|E_0|^2 , \tag{2}$$

where c is the speed of light and ε_0 is the vacuum permittivity. Intensity is the most fundamental physical quantity governing the efficiency of light-matter interaction. Since intensity determines the generation rate of photoinduced carriers, photodetection typically relies on carrier generation and collection to produce an electrical readout. Conventional photodetectors, such as devices based on silicon, InGaAs, and HgCdTe, primarily respond to the intensity of incident light[60–65]. Their output arises from mechanisms including the photovoltaic effect (PVE), photoconductive effect (PCE), photogating effect (PGE), and photothermoelectric effect (PTE)[66–70].

2.2 Wavelength

The wavelength characterizes the spatial periodicity of light and determines its color, photon energy, and propagation behavior. The wavelength λ is related to the wave number k by

$$k=\frac{2\pi}{\lambda} , \tag{3}$$

and the angular frequency ω is linked to the wavelength through the dispersion relation:

$$\omega=\frac{2\pi c}{\lambda} . \tag{4}$$

Accordingly, the photon energy is

$$E_{\rm ph}=\hbar\omega , \tag{5}$$

where $\hbar$ denotes the reduced Planck constant. Wavelength governs not only phase evolution but also light-matter interactions. Since different wavelengths interact with materials through distinct absorption probabilities or resonances, photodetectors commonly employ bandgap engineering or resonance-based structures to achieve spectral selectivity[71–74]. Representative systems include bandgap-tunable materials (GaAsSb, InGaAs, perovskite quantum dot) and microcavities, photonic crystals, and plasmonic structures, enabling wavelength discrimination through selective absorption or resonance enhancement[75–80].

2.3 Polarization

Polarization describes the oscillation direction of the electric field in the transverse plane and represents an intrinsic degree of freedom of light. The polarization state can be expressed using a unit polarization vector:

$$\hat{\boldsymbol{e}}=\cos\alpha\hat{\boldsymbol{x}}+e^{i\delta}\sin\alpha\hat{\boldsymbol{y}} , \tag{6}$$

where α defines the central oscillation axis, and δ represents the phase difference between two orthogonal components. When $\delta=0$, the light becomes linearly polarized, with the electric field oscillating along a fixed direction. For $\delta=\pm\pi/2$ and equal-amplitude components, the field becomes left circular polarization (LCP) and right circular polarization (RCP), corresponding to a spin angular momentum (SAM) of $S_Z=\pm\hbar$ per photon. If the amplitudes are unequal or the phase difference deviates from $\pm\pi/2$, the field is elliptically polarized.

Polarization can also be represented using a second, experimentally common and fully equivalent description—the Stokes parameters：

$$\begin{cases} S_0=|E_x|^2+|E_y|^2 \\ S_1=|E_x|^2-|E_y|^2 \\ S_2=2E_xE_y\cos\delta \\ S_3=E_xE_y\sin\delta \end{cases} . \tag{7}$$

E_x and E_y represent the electric field amplitudes in the x and y directions, respectively, and δ denotes the phase difference between the x and y components. In this representation, linear polarization is characterized predominantly by S_1 and S_2:S_1 distinguishes horizontal from vertical polarization, and S_2 differentiates between 45° and 135° states. Circular polarization (CP) is fully described by S_3, whose sign denotes handedness and whose magnitude reflects the degree of circularity.

Because polarization interacts selectively with anisotropic or symmetry-broken structures, polarization detection often relies on conccg selective detection of linear and CP[81–86].

2.4 Orbital angular momentum

OAM characterizes the helical wavefront of light and constitutes a spatial degree of freedom. The helical phase term：

$$E(\phi)=e^{i\ell\phi} . \tag{8}$$

Different values of ℓ correspond to helical phases of other orders, whose spatial modes are mutually orthogonal and thus support high-dimensional mode spaces. Conventional OAM detection typically relies on bulky optical components such as spiral phase plates or fork gratings[87–89]. Recently, the orbital photogalvanic effect (OPGE: a strictly OAM-dependent photocurrent response, typically found in topological semimetals) in topological semimetals and in photodetector structures with strong spin–orbit coupling has enabled direct electrical readout of OAM information, offering new routes for on-chip OAM detection[90–92].

In summary, the optical field expression integrates intensity, wavelength, polarization, and OAM into a single framework. These quantities appear through the field amplitude, wave number, polarization vector, and helical phase, respectively. This formulation establishes the theoretical basis for studying multidimensional field manipulation, light-matter interactions, and high-dimensional photodetection mechanisms.

2.5 Figures of merit for multidimensional detection

The translation of the aforementioned optical dimensions into readable electrical signals is the core function of any photodetector. To objectively evaluate and compare the performance of different device architectures, a rigorous set of quantitative standards is required. These "Figures of Merit" (FoMs) not only characterize the fundamental efficiency and noise limits of the conversion process but also define the system's capability to discriminate between coupled optical degrees of freedom. Here, we summarize the universal metrics essential for benchmarking multidimensional photodetection.

Responsivity (R): quantifies the conversion efficiency from optical power to electrical signal.

$$R = \frac{I_{\rm ph}}{I_{\rm in}} , \tag{9}$$

where $I_{\rm ph}$ is the photocurrent and $I_{\rm in}$ is the incident power.

Specific detectivity (D^*): evaluates the weakest detectable signal normalized by device area (A) and bandwidth (Δf).

$$D^* = \frac{\sqrt{A\Delta f}}{N_{\rm EP}} , \tag{10}$$

where $N_{\rm EP}$ is the noise equivalent power.

Polarization ratio (PR): measures the selectivity for linear polarization (LP).

$$PR = \frac{I_{\rm max}}{I_{\rm min}} , \tag{11}$$

where $I_{\rm max}$ and $I_{\rm min}$ are the responses to co-polarized and cross-polarized light, respectively.

Circular polarization asymmetry factor (g): quantifies the discrimination capability between LCP and RCP light. It is defined as

$$g = \frac{2\left(R_{\rm L} - R_{\rm R}\right)}{R_{\rm L} + R_{\rm R}} , \tag{12}$$

where $R_{\rm L}$ and $R_{\rm R}$ denote the responsivities to LCP and RCP light, respectively. The value ranges from [−2, 2], with a larger magnitude indicating stronger chiral selectivity.

Stokes parameter accuracy (δS_i): represents the deviation between the measured and incident Stokes parameters S_i (i = 0–3), reflecting the overall fidelity of full-Stokes reconstruction.

Polarization resolution ($\Delta\theta$): the minimum change in the angle of linear polarization (AoLP: the orientation angle of the major axis of the polarization ellipse relative to a reference axis) that the system can distinguish.

Spectral resolution ($\Delta\lambda$): defines the ability to distinguish adjacent wavelengths, often limited by the Q-factor of the integrated resonators or the reconstruction algorithm.

Spectral rejection ratio (RR): evaluates the wavelength selectivity of the device, defined as the ratio of the peak responsivity ($R_{\rm peak}$) to the out-of-band response ($R_{\rm off}$):

$$RR_{\rm dB} = 10\lg\left(\frac{R_{\rm peak}}{R_{\rm off}}\right) \text{ or } RR_{\rm linear} = \frac{R_{\rm peak}}{R_{\rm off}} . \tag{13}$$

High rejection ratios are essential for accurate target identification in complex spectral backgrounds.

3 Physical and computational frameworks for multidimensional perception

3.1 Mathematical formulation of the inverse problem

Instead of treating photodetection merely as a discrete photon-to-electron conversion event, modern multidimensional sensing is fundamentally an information retrieval process governed by the theory of linear systems[93]. Mathematically, the interaction between the incident light field and the detector can be rigorously modeled as a linear mapping. Let the incident light field be represented by a vector $\boldsymbol{x} \in \mathbf{R}^N$ (containing parameters such as spectral bins λ, Stokes parameters S, or OAM modes l), where N denotes the dimensionality of the optical information (i.e., the number of physical degrees of freedom). The measured electrical signals by a vector $\boldsymbol{y} \in \mathbf{R}^M$, where M denotes the number of measurement channels (i.e., the dimensionality of the output signal). The entire sensing process is described by the equation:

$$\boldsymbol{y} = \boldsymbol{M}\boldsymbol{x} + \boldsymbol{n} , \tag{14}$$

where $\boldsymbol{M} \in \mathbf{R}^{M\times N}$ represents the instrument matrix (or response matrix), determined by the device's physical response functions, and $\boldsymbol{n}$ denotes the stochastic noise.

In traditional single-pixel detectors, the design goal is typically a scalar response, with $\boldsymbol{M}$ approximating an identity matrix to achieve perfect decoupling. However, in integrated multidimensional detectors, the distinct optical dimensions are often physically coupled, resulting in a non-diagonal $\boldsymbol{M}$. The core challenge thus becomes the inverse

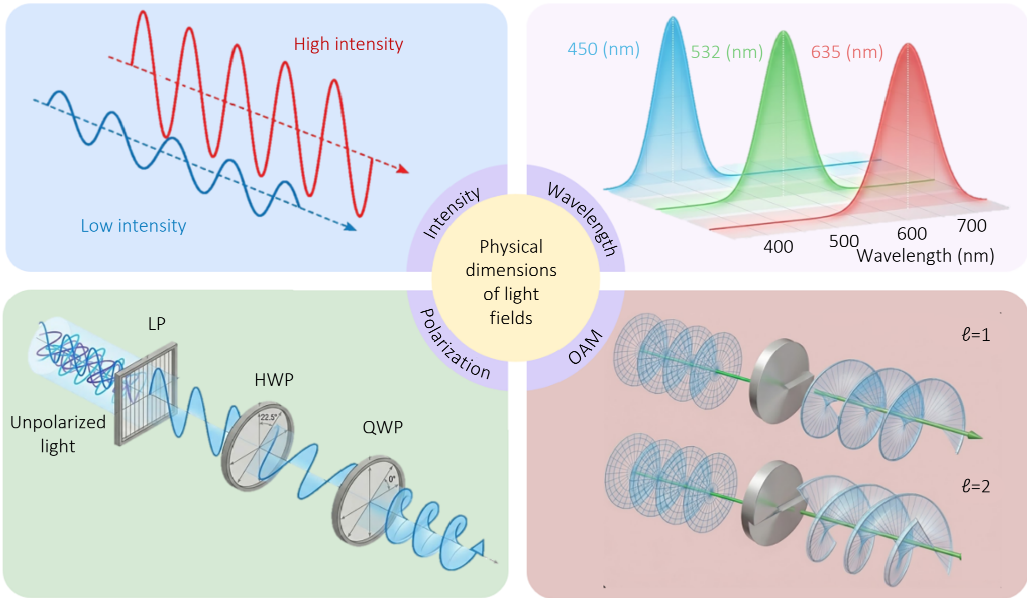

Fig. 2 | Physical dimensions of light fields.

problem: retrieving the unknown state $\boldsymbol{x}$ from the measured vector $\boldsymbol{y}$ (i.e. $\widehat{\boldsymbol{x}} = \boldsymbol{M}^{-1}\boldsymbol{y}$). The accuracy of this retrieval is theoretically bounded by the condition number ($\kappa(\boldsymbol{M})$) of the matrix. A well-designed hardware structure (frontend encoding) minimizes $\kappa(\boldsymbol{M})$ to prevent noise amplification, while intelligent algorithms (backend decoding) optimize the estimation of $\widehat{\boldsymbol{x}}$ even when the system is underdetermined ($M < N$)[94].

3.2 Hardware strategies for optical information encoding

To decouple the entangled optical information, the hardware's primary task is to break the symmetry of the photoresponse, thereby ensuring that the columns of M are linearly independent. We categorize the encoding architectures into three paradigms.

3.2.1 Spatial-division multiplexing

Spatial-Division Multiplexing (SDM) utilizes geometric diversity to map orthogonal optical states onto distinct spatial ports or pixels[95,96]. Mechanistically, this is achieved by engineering asymmetric electrode layouts or utilizing intrinsic material dichroism to force photons with specific polarization or OAM states to be absorbed at different spatial locations. The primary advantage of this architecture is its ability to enable single-shot detection, which is crucial for capturing ultrafast dynamics or tracking moving targets without temporal latency. As discussed in subsequent sections, low-symmetry materials such as BP (Section 4) naturally support this mechanism, while metasurfaces (Section 5) can employ "super-pixel" designs to achieve arbitrary spatial projections of high-dimensional vectors[97,98]. Furthermore, disordered scattering media can also serve as efficient SDM encoders by mapping wavelengths to unique speckle patterns[99].

3.2.2 Time-division multiplexing

In contrast to spatial approaches, Time-Division Multiplexing (TDM) leverages the temporal tunability of active materials to capture information sequentially within a single pixel[28]. By dynamically modulating external parameters—such as the gate voltage (V_g), bias polarity, or mechanical strain—the spectral responsivity $R(\lambda)$ or polarization preference of the device is altered over distinct time frames (t_1, t_2, $\cdots$, t_M)[100−102]. This process effectively constructs the measurement matrix $\boldsymbol{M}$ row by row over time[103]. While TDM inevitably trades temporal resolution for spatial compactness, it is ideal for high-density integration where minimizing the footprint is the primary constraint. However, it is crucial to note the trade-offs in applicability. While TDM minimizes the footprint, the required serial modulation introduces temporal latency. Consequently, such architectures are generally unsuitable for dynamic scenarios—such as tracking fast-moving targets or high-speed optical communications—where the signal state may evolve faster than the modulation cycle. For these time-critical applications, single-shot SDM architectures (Section 3.2.1) remain the preferred solution.

3.2.3 Photonic network-on-chip encoding

Moving beyond discrete device units, silicon photonic architectures enable pre-detection optical computing. In this paradigm, waveguide meshes, Mach-Zehnder interferometers (MZIs), and inverse-designed diffractive elements are employed to perform unitary transformations, such as mode sorting and wavelength demultiplexing, directly in the optical domain before the light reaches the photodiode[104]. This approach shifts the complexity from the material level to the circuit level, representing the system-level integration discussed in Section 6, where "sensing" and "computing" merge on the silicon-on-insulator (SOI) platform.

3.3 Computational frameworks for reconstruction and design

Once the multidimensional information is encoded into electrical signals $\boldsymbol{y}$, the final step is accurate reconstruction. The choice of the decoding algorithm depends strictly on the mathematical properties of $\boldsymbol{M}$ and the sparsity of the target signal $\boldsymbol{x}$.

3.3.1 Analytical reconstruction

For systems designed with high orthogonality, such as those employing polarizing beam splitter-like structures, the instrument matrix $\boldsymbol{M}$ is well-conditioned ($\kappa \approx 1$). In such cases, the optical parameters can be retrieved via direct linear algebra, typically using the Moore-Penrose pseudoinverse. This deterministic approach offers the lowest computational latency and provides physically interpretable results, making it highly suitable for real-time sensing applications. However, its accuracy relies heavily on the precise calibration of $\boldsymbol{M}$, rendering it susceptible to fabrication errors that cause the actual physical response to deviate from the design.

3.3.2 Optimization and inverse design strategies

When the sensing problem exceeds the capability of simple linear inversion—either due to an under-determined system ($M < N$) or a complex physical mapping—optimization algorithms become the core engine. This approach plays a dual role in modern perception: as a solver for signal reconstruction and as an architect for hardware design.

In signal reconstruction for underdetermined systems, compressive sensing (CS) algorithms incorporate regularization terms, such as L1-norm minimization, to enforce sparsity and recover high-dimensional data from limited measurements[105]. Similarly, in nonlinear detection scenarios such as spectroscopic ellipsometry, iterative optimization techniques are employed. Instead of a direct inverse, these algorithms iteratively update the estimated parameters to minimize the error function between the theoretical model and the measured data.

Beyond reconstruction, optimization is increasingly applied to the design of the instrument matrix $\boldsymbol{M}$ itself. In complex photonic circuits, the mapping from geometric parameters to optical response is non-intuitive. Here, inverse design (topology optimization) is utilized to computationally "evolve" the device structure, creating compact components with customized functionalities[106]. Additionally, optimization algorithms are used to explicitly minimize the condition number of the sensing matrix, ensuring that the measurement channels are as orthogonal as possible to reduce noise amplification during retrieval.

3.3.3 Deep learning and physics-informed decoding

For complex systems where $\boldsymbol{M}$ is difficult to model explicitly due to scattering, disorder, or extreme nonlinearity, data-driven approaches have become the prevailing solution. Deep Neural Networks (DNNs) learn the statistical mapping $\mathcal{F}: y \longrightarrow x$ from massive datasets, effectively bypassing the need for an explicit physical model[107–109]. A promising trend in this domain is the emergence of physics-informed neural networks (PINNs), which embed physical constraints (e.g., energy conservation, Maxwell's equations) into the network's loss function[110,111]. This ensures that the reconstruction is not only accurate but also physically rigorous.

3.4 Calibration and error analysis

The theoretical validity of the reconstruction $\widehat{\boldsymbol{x}} = \boldsymbol{M}^{-1}\boldsymbol{y}$ fundamentally relies on the accuracy of the instrument matrix $\boldsymbol{M}$ and the signal-to-noise ratio of the measurement. In practical integrated systems, however, deviations are inevitable, necessitating a rigorous error analysis to define the physical limits of perception.

First, systematic errors arise from the discrepancy between the ideal designed matrix and the actual physical response. Fabrication tolerances—such as nanometer-scale variations in metasurface geometry—and environmental drifts like temperature-induced spectral shifts introduce a perturbation term $\Delta\boldsymbol{M}$ (defined as the deviation between the actual instrument matrix and the ideal designed matrix). To prevent these deviations from translating into reconstruction artifacts, a rigorous Calibration Phase is mandatory. By mapping the system response against known standard states (e.g., using a tunable laser or polarization state generator), the "real" $\boldsymbol{M}$ can be experimentally determined to correct the forward model.

Beyond systematic errors, stochastic noise $\boldsymbol{n}$—including shot noise, thermal noise, and readout circuit noise—imposes a more fundamental limit. Unlike systematic errors, stochastic noise cannot be eliminated by calibration; instead, its impact is amplified by the system's condition number $\kappa(\boldsymbol{M})$. The relative error in the final reconstruction is mathematically bounded by the product of the condition number and the noise level. This relationship highlights a critical design principle for multidimensional detectors: minimizing $\kappa(\boldsymbol{M})$ through optimized frontend encoding (as discussed in Section 3.2) is just as vital as suppressing device noise. Ultimately, a well-conditioned matrix ensures that the system remains robust against experimental uncertainties, defining the precision frontier of intelligent perception.

To provide a holistic view of this computational sensing pipeline, Fig. 3 illustrates the synergistic integration of hardware encoding strategies, error calibration protocols, and intelligent reconstruction algorithms.

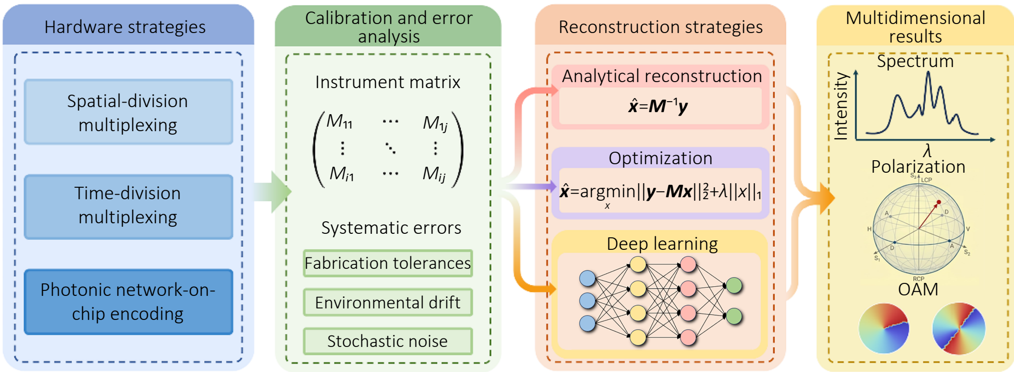

Fig. 3 | Signal readout architectures and intelligent reconstruction strategies.

4 Photodetectors based on intrinsic material properties

2D materials enable the manipulation of multidimensional optical fields through fundamental light-matter interactions. Intrinsic properties—such as crystal symmetry, electronic band structure, and carrier transport—dictate how specific optical degrees of freedom couple with the material[112–114]. By harnessing these mechanisms, photodetectors can directly convert optical inputs into electrical signals. Consequently, devices operating on these principles form the essential building blocks of integrated optoelectronic detection systems. This section investigates how to achieve multidimensional optical field detection by optimizing these foundational units.

4.1 Intrinsic property-enabled single-dimensional photodetectors

As the most fundamental dimension of photodetection, optical intensity detection has evolved from initial functional realization to performance-oriented optimization. However, detectors based on 2D materials remain constrained by intrinsic limitations, such as inefficient carrier transport and weak light absorption[115]. To address these issues, Wang et al. designed a BP/$MoTe_2$/BP tunneling heterostructure integrated with an Au reflector (Fig. 4(a))[116]. By combining the carrier-blocking capability of the $MoTe_2$ barrier to suppress dark current with optical interference enhancement provided by the Au reflector, the device achieved a high responsivity of 4 $A\cdot W^{-1}$ and a specific detectivity of 3.0×10^{10} Jones. Similarly, targeting dark current suppression, Chen et al. employed unipolar barrier architectures (WS_2/h-BN/$PdSe_2$ nBn and BP/MoS_2/graphene pBp) based on vdWHs (Fig. 4(b))[117]. By engineering band alignments to block majority carriers while allowing photogenerated carriers to flow unimpeded, they achieved high detectivity in both the visible and mid-wave infrared bands.

Optical intensity detection captures no wavelength information, necessitating a transition to spectral sensing. To address this without bulky dispersive optics, electrically tunable detectors have emerged as a key strategy for miniaturized spectrometry[118]. Yuan et al. demonstrated a wavelength-scale spectrometer utilizing a single tunable BP photodetector (Fig. 4(c)). By leveraging the giant Stark effect to modulate the photoresponse spectrum via gate voltage and employing a "learning" algorithm based on blackbody radiation, they achieved spectral reconstruction in the 2–9 μm mid-infrared range[100]. In contrast, Yoon et al. developed a miniaturized spectrometer based on a gate-tunable MoS_2/WSe_2 heterojunction, achieving a spectral resolution of 3 nm across the 405–845 nm range (Fig. 4(d))[119]. This device reconstructs incident spectra from gate-modulated photoresponses via computational algorithms. However, it is crucial to note that this reconstruction involves solving a Fredholm integral equation of the first kind, which is mathematically ill-posed and highly sensitive to noise. Consequently, the reliance on regularization terms (e.g., Tikhonov regularization) to stabilize the solution introduces implicit smoothness priors, potentially limiting the system's ability to resolve complex spectral features containing sharp peaks or high-frequency components. Collectively, these studies highlight the unique advantages of 2D materials for compact, wavelength-resolved photodetection.

Beyond intensity and wavelength, polarization conveys critical optical information. Low-symmetry 2D materials, such as BP and tellurium (Te), are ideal candidates for addressing this parameter. Unlike isotropic graphene and MoS_2, these materials exhibit intrinsic in-plane anisotropy and pronounced linear dichroism. This anisotropy establishes the physical basis for efficient, filter-free polarization detection. Building on this principle, Yuan et al. achieved broadband linear-polarization detection from the visible to the mid-infrared using a vertical BP p-n junction (Fig. 4(e))[120]. Tong et al. confirmed the strong infrared anisotropy and excellent environmental stability of Te, originating from its helical atomic chain structure (Fig. 4(f))[121]. Despite these advantages, direct polarization detection often exhibits a limited extinction ratio. To address this challenge, He et al. introduced a gate-controlled anisotropy

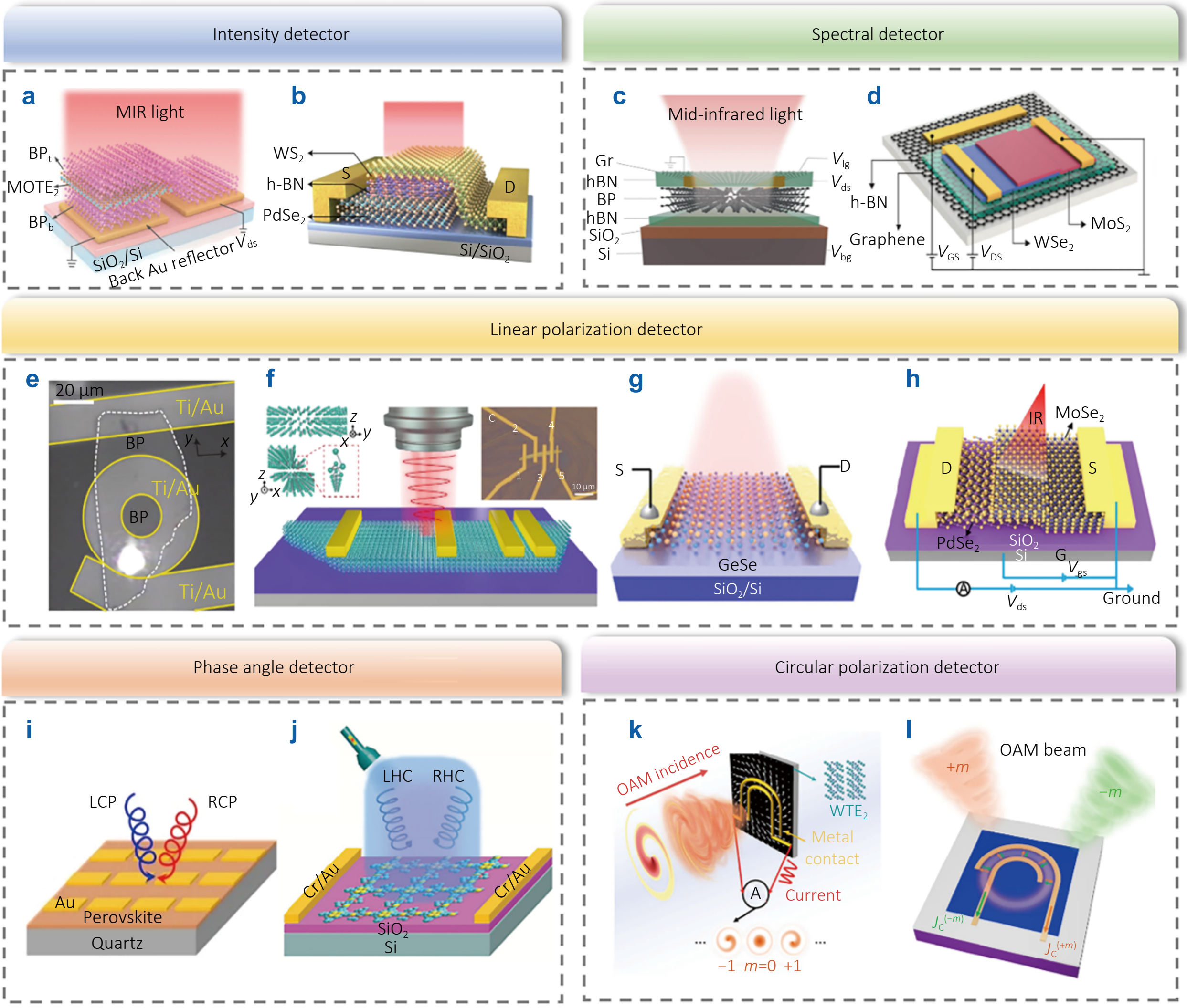

Fig. 4 | Single-dimensional optical field detectors based on intrinsic properties of materials. (a) Schematic diagram of the $BP_t/MoTe_2/BP_b$ bipolar-barrier tunnel heterostructure. (b) Schematic diagram of the WS_2/h-BN/$PdSe_2$ nBn vdW unipolar barrier photodetector. (c) Schematic of the BP spectrometer. (d) MoS_2/WSe_2 heterojunction spectrometer. (e) BP photodetector with a ring-shaped photocurrent collector. (f) GeSe photodetector. (g) Structure schematic of the MSM-type GeSe photodetector. (h) Schematic of a $MoSe_2/PdSe_2$ heterostructure device. (i) The device of (R- and S-α-PEA)PbI_3 film photodetector. (j) Schematic illustration of the photodetector based on CityU-7 and CityU-8 for CPL detection. (k) Schematic of the photocurrent measurement from optical beams carrying OAM. (l) Schematic of the radial OPGE response collected by an OAM detector with U-shaped electrodes. Figure reproduced from: (a) ref.[116], Nature Publishing Group; (b) ref.[117], Nature Publishing Group; (c) ref.[100], American Association for the Advancement of Science; (d) ref.[119], American Association for the Advancement of Science; (e) ref.[120], Nature Publishing Group; (f) ref.[121], Nature Publishing Group; (g) ref.[122], Wiley-VCH; (h) ref.[123], Nature Publishing Group; (i) ref.[124], Nature Publishing Group; (j) ref.[125], Wiley-VCH; (k) ref.[90], American Association for the Advancement of Science; (l) ref.[92], Nature Publishing Group.

modulation strategy in GeSe, significantly enhancing the *PR* to 54.8 (Fig. 4(g))[122]. Polarization detection can also be extended to broader spectral ranges. Liu et al. designed a broadband polarization-sensitive photodetector based on a $MoSe_2/PdSe_2$ heterostructure, achieving operation from the near-infrared (NIR) to the long-wave infrared (LWIR) (Fig. 4(h))[123]. The device features low noise current, low power consumption, and high detectivity. Benefiting from photogating-assisted tunneling, it delivers a responsivity of ~8 × 10^4 A/W and a response speed of 590 ns under NIR illumination. Alongside the continuous improvement of linear polarization detection, the sensing of CP has also been extensively explored. Chen et al. developed a circularly polarized light detector based on a chiral organic-inorganic hybrid perovskite ((α-PEA)PbI_3). The device achieves a responsivity of 797 mA/W and a specific detectivity of 7.1 × 10^{11} Jones at 395 nm (Fig. 4(i))[124]. Gu et al. further demonstrated a CP g-factor of 0.5 at 405 nm using 2D covalent organic frameworks (COFs) (Fig. 4(j))[125].

With the maturation of polarization detection technology, the research frontier is expanding toward OAM detection. Conventional approaches rely on bulky diffractive elements to resolve helical phase wavefronts, hindering device miniaturization. Recently, on-chip OAM detectors based on the OPGE have overcome this limitation by enabling direct electrical readout. This concept was first introduced by Ji et al., who used the type-II Weyl semimetal WTe_2, where broken inversion symmetry allows the OAM-induced phase gradient to be converted into a radial photocurrent (Fig. 4(k))[90]. More recently, Sun's group realized OAM detection in wafer-scale multilayer graphene, overcoming the instability of topological semimetals, achieving an order-of-magnitude performance enhancement, and preserving excellent CMOS compatibility (Fig. 4(l))[92].

4.2 Intrinsic mechanism-enabled multidimensional photodetectors

While single-dimensional detection is mature, progress toward multidimensional fusion requires extracting distinct optical parameters within a unified framework. To eliminate the need for bulky external optics, emerging strategies leverage intrinsic material engineering, such as heterostructures and moiré superlattices. These approaches enable ultracompact, single-device detection. This section systematically reviews these mechanisms, ranging from joint polarization–intensity and full-Stokes detection to polarization-wavelength and three-dimensional fusion.

The development of multidimensional photodetection begins with the joint measurement of polarization and intensity. Here, the primary challenge involves reconciling conflicting physical demands: accurate intensity sensing requires isotropic absorption, whereas polarization resolution necessitates strong anisotropy. To address this issue via the SDM strategy, Xiong et al. vertically stacked an isotropic $BiSe_3$ layer for power calibration with twisted BP layers for polarization analysis (Fig. 5(a))[126]. This architecture physically separates the intensity and LP signals into different layers, thereby enabling effective decoupling. To achieve a more compact integration of intensity and LP sensing, researchers developed a temporal multiplexing strategy based on bias-tunable carrier transport. Using a b-AsP/WS_2/b-AsP (b-AsP: black arsenic phosphorus) heterostructure, Deng et al. demonstrated that switching the bias polarity enables a single device to independently obtain full-angle polarization states and intensity information in the mid-infrared regime, with successful polarization imaging (Fig. 5(b, c))[127]. To further advance this TDM architecture, Ma et al. designed a $PdSe_2/MoS_2/PdSe_2$ heterostructure detector (Fig. 5(d, e))[128]. A detector that not only retrieves both the AoLP and degree of linear polarization (DoLP: the ratio of the intensity of the linearly polarized component to the total light intensity, characterizing the purity of linear polarization.) across a broad spectral range via bias switching, but also exhibits bipolar photoresponse at zero bias, enabling more efficient polarization imaging and encoded communication.

Advancing to full-Stokes detection requires resolving CP. However, mirror symmetry within linearly anisotropic materials inherently suppresses CP. Consequently, realizing single-device detection requires introducing symmetry-breaking mechanisms or chirality-dependent interactions. Fang et al. addressed this challenge by implementing a geometric SDM strategy using an SL-MoS_2/FL-MoS_2 homojunction, where the built-in electric field amplifies the nonlinear circular photogalvanic effect (CPGE: a photocurrent response where the current direction depends on the helicity of the incident circularly polarized light.) (Fig. 5(f, g))[129]. By combining this chirality-sensitive nonlinear response with the material's intrinsic linear anisotropy, the device retrieves all four Stokes parameters, including the total intensity S_0, under zero bias. To reduce fabrication complexity, Ge et al. introduced a backend deep learning decoding strategy based on polycrystalline perovskite films with randomly oriented grains (Fig. 5(h))[130]. By employing deep learning, the system maps the spatially random linear and circular dichroism responses to the Stokes vector, enabling high-precision single-shot full-Stokes imaging. However, this strategy fundamentally relies on stochastic calibration rather than deterministic optical design. Since the response matrix originates from random grain distributions, the sensing mechanism is inherently device-specific, meaning the accurate reconstruction is contingent on the algorithm strictly memorizing the random mapping of each individual device.

Following full-Stokes detection, simultaneous wavelength and polarization resolution is critical for comprehensive optical characterization. However, polarization selectivity in most optoelectronic materials is often accompanied by wavelength-dependent absorption. Zhang et al. employed a TDM band-structure engineering approach and constructed a misaligned unipolar-barrier photodetector based on b-AsP. By tuning the bias voltage to control carrier transport across the anisotropic barrier, the device achieves switchable spectral bands and distinct polarization sensitivities, allowing wavelength and polarization to be independently identified (Fig. 6(a))[131]. To advance intelligent sensing, Tang et al. developed an adaptive TDM sensor based on moiré superlattices, in which the interlayer twist angle generates wavelength-dependent, polarization-sensitive optical resonances (Fig. 6(b))[132]. By modulating the moiré potential, the device enables adaptive spectro-polarimetric hyper-imaging with simultaneous access to fine spatial and spectral features via CS reconstruction. This strategy illustrates how moiré engineering can transform simple 2D materials into advanced platforms for computational imaging. To further achieve the simultaneous extraction of wavelength and full-Stokes parameters, Ma et al. utilized twisted double-bilayer graphene to exploit the gate-tunable bulk photovoltaic effect (BPVE: a zero-bias photocurrent generation mechanism in

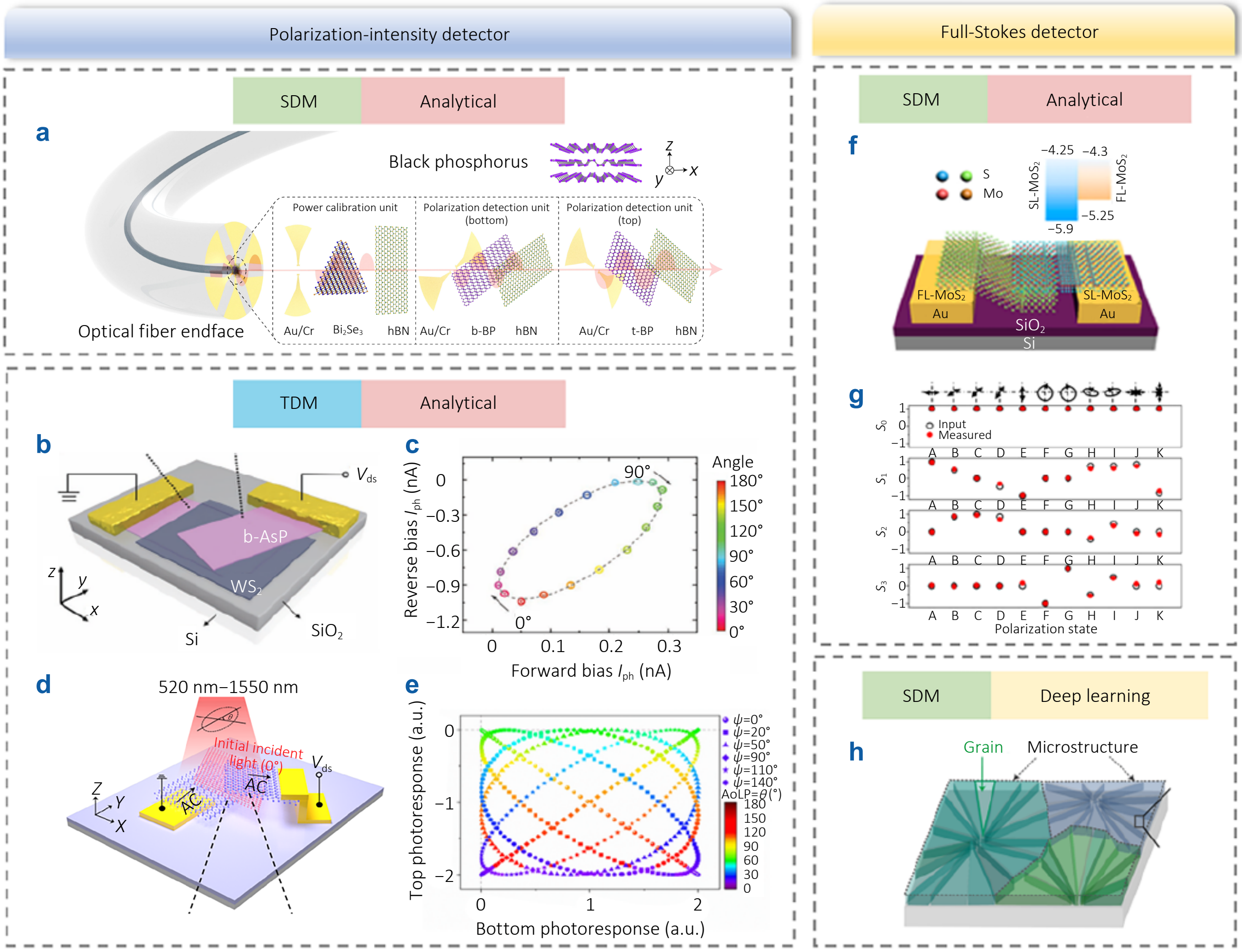

Fig. 5 | Material-based polarization-intensity detector and full-stokes detectors. (a) Schematic illustration of the designed fiber-integrated polarimeter. (b) Schematic diagram of the unipolar barrier vdWH photodetector. (c) 2D plots of forward bias I_{ph1} and reverse bias Iph_2 in the Cartesian coordinate system. (d) Schematic illustration of the $PdSe_2/MoS_2/PdSe_2$ vdWH. (e) 2D plots of the bottom and top photoresponses. (f) $SL\text{-}MoS_2/FL\text{-}MoS_2$ homojunction device. (g) Stokes parameters (S_0–S_3) under different input polarized light excitation. (h) $PdSe_2/2H\text{-}MoTe_2$ vdWH photodetector. Figure reproduced from: (a) ref.[126], American Association for the Advancement of Science; (b, c) ref.[127], Wiley-VCH; (d, e) ref.[128], Wiley-VCH; (f, g) ref.[129], Nature Publishing Group; (h) ref.[130], Nature Publishing Group.

non-centrosymmetric materials driven by the geometric phase of electronic wavefunctions.) arising from moiré quantum geometry (Fig. 6(c, d))[133]. By combining distinct gate-dependent photovoltage responses with deep learning reconstruction, the device retrieves full-Stokes polarization information and wavelength signatures from a single-pixel output. While this highlights the convergence of topological physics and AI, it is worth noting that retrieving multiple independent optical parameters from a single geometric structure imposes strict orthogonality requirements on the response functions. Consequently, the readout accuracy is fundamentally limited by the condition number of the measurement matrix formed by these tunable states, rendering the system susceptible to noise when resolving spectrally or polarization-mixed states.

As spectral-polarization fusion matures, the research frontier is shifting toward higher-dimensional integration. The simultaneous resolution of intensity, polarization, and wavelength marks a significant advancement; however, it faces substantial challenges. The primary obstacle is the overlap of response mechanisms, which complicates the effective acquisition of multidimensional information within a single device. To address these demands using a compact SDM architecture, Wang et al. developed a twisted b-AsP homojunction, where arsenic alloying enables continuous bandgap tuning and thus introduces spectral sensitivity (Fig. 6(e, f, g))[134]. Interlayer band coupling at the twisted interface generates distinct photoresponse patterns jointly determined by photon energy and polarization orientation. Coupled with its intrinsic dual-polarity output, the device enables the simultaneous analytical extraction of intensity, spectral, and polarization information within a single measurement. Beyond 2D material stacking, perovskite

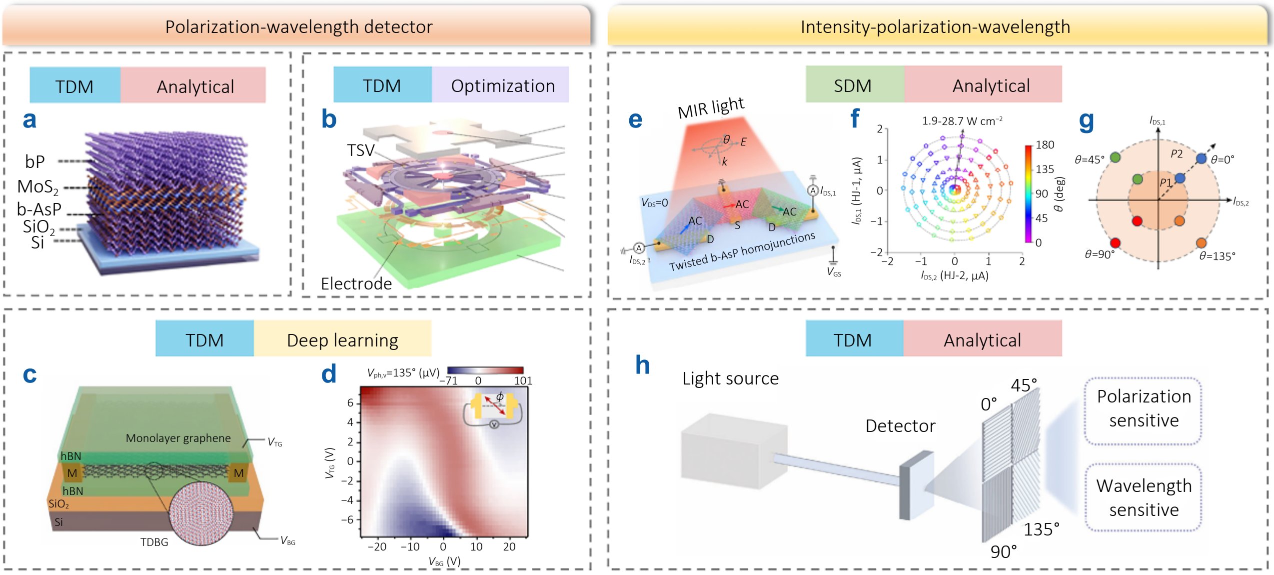

Fig. 6 | Material-based polarization-wavelength detectors and intensity-polarization-wavelength detectors. (a) Schematic of the device, composed of vertically stacked b-AsP/MoS_2/bP heterostructure. (b) Schematic of the primary components in the MEMS-TMPhC sensor. (c) Schematic of the TDBG photodetector. (d) Dual-gate controlled photocurrent contribution spectrum under spectral-polarization response. (e) Three-angle b-AsP multi-dimensional detector structure. (f) 2D plots of predicted $I_{DS,1}$ and $I_{DS,2}$ at different polarization angles (θ) and incident intensities (P). (g) 2D plots of photocurrents measured from the double twisted b-AsP homojunctions. (h) Working mechanism of the polarization- and spectrum-sensitive photodetector. Figure reproduced from: (a) ref.[131], Nature Publishing Group; (b) ref.[132], American Association for the Advancement of Science; (c, d) ref.[133], Nature Publishing Group; (e–g) ref.[134], Nature Publishing Group; (h) ref.[135], Wiley-VCH.

systems offer an alternative route through programmable structural engineering. Guo et al. developed a TDM-enabled multidimensional detector based on composition-graded perovskite nanowire arrays, in which composition-dependent band gaps provide spectral selectivity, and geometric anisotropy imparts polarization sensitivity (Fig. 6(h))[135]. Importantly, by employing electric-field-induced dynamic band modulation, the device generates distinguishable transient photoresponses that support single-shot retrieval of intensity, spectral, and polarization parameters.

In summary, Section 4 systematically explored photodetection strategies governed by intrinsic material properties. Ranging from engineered band alignments in vdWHs to topological control in moiré superlattices, these approaches have enabled the extraction of single-dimensional parameters and the preliminary fusion of multidimensional information, such as polarization and wavelength.

5 Photodetectors enabled by metasurface engineering

While the intrinsic properties of materials discussed in Section 4 provide the foundation for photodetection, they often face inherent constraints such as limited optical absorption and fixed crystallographic symmetry. To transcend these material-specific boundaries, metasurface engineering has emerged as a versatile platform that significantly expands the design space by acting as a functional interface to reshape light-matter interactions[136–138]. By rigorously engineering the subwavelength geometry and orientation of meta-atoms, these structures enable the precise tailoring of local electromagnetic environments far beyond the restrictions of natural lattice structures[139–141]. This paradigm effectively integrates metasurface-driven manipulation with material-based conversion, shifting photodetection from passive sensing to active optical field encoding. Consequently, this section examines how metasurface-enabled architectures enable photodetection systems to evolve from simple performance enhancement to integrated detection and fusion of multidimensional optical information.

5.1 Metasurface-enabled single-dimensional photodetectors

In single-dimensional photodetection, device performance is fundamentally constrained by the intrinsic properties of the materials. The light absorption of atomically thin layers is limited by their band structure and physical thickness, resulting in inherently low efficiency. Meanwhile, the weak natural birefringence or anisotropy of most materials restricts the achievable polarization extinction ratio. To overcome these limitations, metasurfaces are introduced to reshape the local electromagnetic environment at the device interface. By exploiting localized surface plasmon resonances (LSPR) and dielectric Mie resonances, or by designing anisotropic or chiral meta-atoms, metasurfaces can selectively and substantially enhance the response along a single optical dimension. This section systematically discusses how metasurface design enables significant improvements in key performance metrics, including responsivity, spectral resolution, and polarization extinction ratio.

Enhancing light-matter interaction is the primary goal of metasurface integration, particularly for overcoming the limited absorption efficiency of 2D materials. To address this challenge, Jiang et al. proposed a synergistic potential-well engineering strategy. The engineered potential well functions as a resonant cavity that traps photons and confines photogenerated carriers, effectively suppressing recombination losses (Fig. 7(a))[142]. As a result, the device achieves a high responsivity of 0.2–38 A/W across the infrared spectrum. Building on this concept, Wu et al. integrated metastructures with vertically stacked vdWHs, enabling efficient coupling between electromagnetic resonances and out-of-plane carrier transport (Fig. 7(b))[143]. This architecture overcomes the room-temperature performance limitations of conventional 2D detectors, achieving sensitivity and response speeds comparable to those of commercial cryogenic HgCdTe devices.

After addressing the efficiency bottlenecks in intensity detection, the unique capabilities of metasurfaces are further utilized to enhance LP sensitivity. Unlike intrinsic crystal lattices, which are constrained by limited dichroism, metasurfaces introduce engineered geometric anisotropy to achieve high polarization extinction ratios. Dai et al. demonstrated this approach by integrating Te nanobelts with a plasmonic metasurface to construct a strongly anisotropic optical response (Fig. 7(c, d))[144]. The device converts polarization-dependent photothermal heating into electrical signals through the PTE effect, achieving an ultrahigh PR of 2.5×10^4 and a responsivity of 410 V/W under zero bias. These results show that metasurface-enabled structured absorption can far surpass the polarization-selectivity limits dictated by intrinsic material properties.

Another notable advantage of metasurfaces is their ability to detect CP, a functionality that conventional 2D materials with mirror symmetry can rarely achieve. Metasurfaces introduce chiral geometries to enable photon-spin detection without external optical components. Li et al. employed

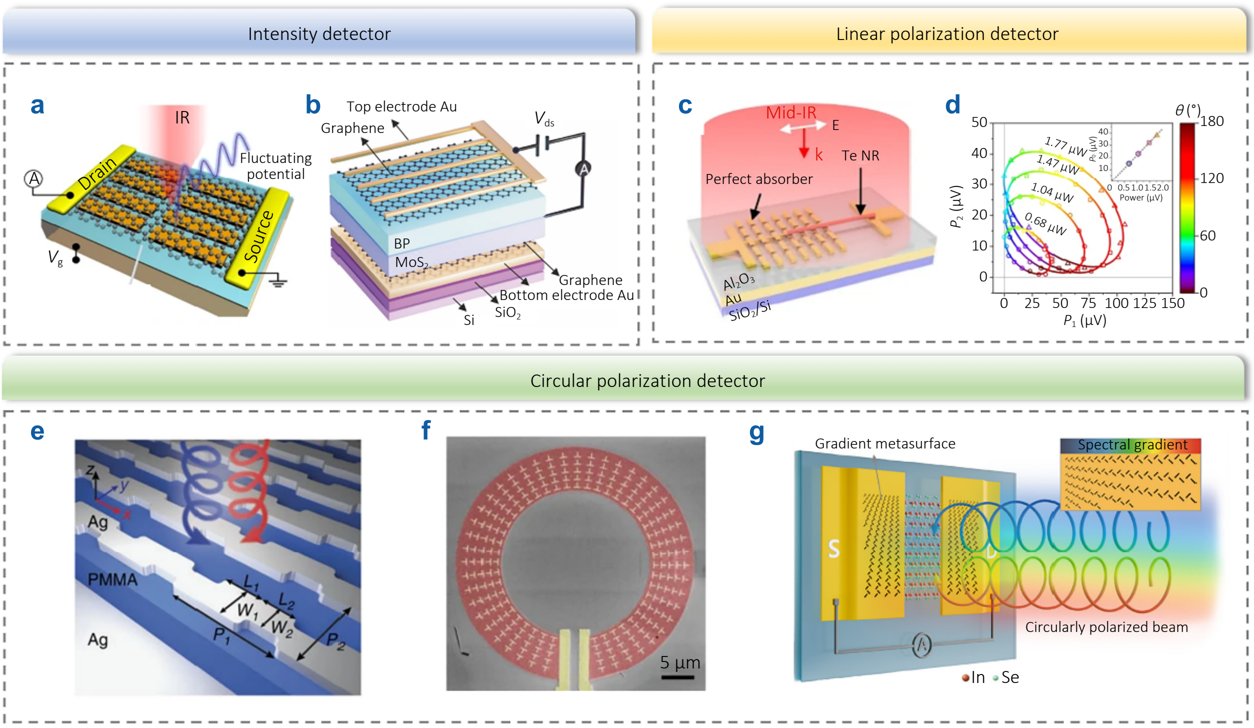

Fig. 7 | Metasurface-based high performance single-dimensional optical field detectors. (a) Illustration of the graphene photodetector with a configurable all-dielectric surface. (b) Schematic illustrating the experimental setup of the Gr/BP/MoS_2/Gr vertical channel photodetector. (c) Polarization-sensitive infrared photothermoelectric detectors. (d) 2D plots of P_1 and P_2 under different linear polarization angles θ and light powers. (e) Schematic of the chiral metamaterial consisting of the chiral plasmonic meta-molecule array, dielectric spacer, and metal backplane. (f) Concept of geometric photodetectors for CPL-specific detection. (g) Device architecture of the broadband CPL photodetector. Figure reproduced from: (a) ref.[142], Nature Publishing Group; (b) ref.[143], Nature Publishing Group; (c, d) ref.[144], Nature Publishing Group; (e) ref.[145], Nature Publishing Group; (f) ref.[146], Nature Publishing Group; (g) ref.[148], Wiley-VCH.

chiral plasmonic metamaterials to selectively excite hot electrons under circularly polarized illumination (Fig. 7(e))[145]. These energetic carriers are injected into the semiconductor, enabling electrical discrimination between LCP and RCP light in the telecommunications band, with a *PR* of 3.4. Wei et al. developed a filter-free mid-infrared spin-resolved photodetector by combining a geometrically arranged, mirror-symmetric plasmonic nanostructure array (T-shaped metasurface) with graphene strips (Fig. 7(f))[146]. The device operates at room temperature, achieving a circular polarization *PR* of up to 84, a zero-bias responsivity of 392 V/W, and an ellipticity detection sensitivity of $0.03°\text{Hz}^{-1/2}$. To overcome the narrow spectral response of plasmonic resonances, Zhang et al. designed a high-contrast, broadband CP detector by integrating all-dielectric achiral V-groove nanostructures with Te nanosheets[147]. This structure converts the near-field modal differences between LCP and RCP light into PTE voltages of opposite sign, achieving a *PR* of about 10^7 at 405 nm and maintaining strong performance across the visible spectrum. Furthermore, our group advanced CP detection by combining vertically aligned nanoslit arrays with InSe to create a zero-bias gradient-metasurface photodetector (Fig. 7(g))[148]. The device generates a unidirectional photocurrent that depends on the handedness of circularly polarized light through surface plasmon excitation, achieving a *PR* of about 1.6×10^4 over a broad range of 500–1100 nm. These developments demonstrate that metasurfaces can effectively convert optical SMA into electrical signals through extrinsic structural engineering, fundamentally surpassing the symmetry constraints of natural materials. To explicitly benchmark these advancements, Table 1 summarizes the key figures of merit for recent polarization-sensitive photodetectors. By comparing metrics such as *PR*, responsivity, and response speed across various intrinsic materials and metasurface designs, the table highlights a critical trend: while intrinsic materials offer advantages in response, metasurface-enhanced architectures achieve significantly higher *PR* and greater design flexibility through structural engineering.

In summary, by tailoring light-matter interactions at the subwavelength scale, metasurfaces serve as a powerful platform for enhancing detector performance. They redefine the performance boundaries of photodetection, effectively transforming weak, non-selective intrinsic material responses into strong, highly discriminative electrical readouts.

5.2 Metasurface-enabled multidimensional photodetectors

As discussed in previous sections, single-dimensional photodetectors have laid a solid foundation for optoelectronics by achieving exceptional sensitivity and response speeds in specific domains. While these devices are indispensable for high-performance signal acquisition, capturing richer information from the optical field necessitates the simultaneous retrieval of multiple independent parameters. Section 4.2 addressed this need through intrinsic material engineering. However, detection capabilities remain limited when relying solely on lattice properties or complex stacking. In this section, we introduce a complementary paradigm: metasurface-enabled multidimensional detection. Unlike intrinsic approaches, metasurfaces utilize extrinsic structural degrees of freedom—such as geometric anisotropy and spatial dispersion—to detect complex optical information[149–155]. Consequently, the discussion proceeds from intensity and polarization detection to full Stokes vector reconstruction and joint wavelength-polarization detection, finally covering the integrated detection of high-dimensional optical fields.

The transition from single-point intensity detection to polarization-resolved sensing is effectively enabled by engineering the geometric anisotropy of meta-atoms to construct customized SDM architecture. This strategy offers greater design flexibility than relying on the intrinsic dichroism of crystal lattices. Wei et al. pioneered a metasurface-mediated graphene photodetector capable of calibration-free polarization detection (Fig. 8(a, b))[156]. By integrating noncentrosymmetric gold nanoantennas with graphene to mimic the artificial BPVE, the device generates a nonlocal

Table 1 | The performance of polarization detector.

Architectures	Materials	Function	Wavelength (μm)	PR or DR	Response time (s)	Responsivity (A/W)	Self-driven	Ref.
Intrinsic materials	BP	LP	0.4–1.7	3.5	40 kHz	350	No	120
	2D-Te	LP	0.52–3.0	8	78×10^{-6}	1.36×10^3	No	121
	2D GeSe	LP	0.8–1	54.8	14×10^{-3}	2	No	122
	$MoSe_2/PdSe_2$	LP	0.78–10.6	15.5	590×10^{-6}	4	Yes	123
Artificial metasurface	Te/Au metamaterials	LP	8	2.5×10^4	176×10^{-6}	410 V/W	Yes	144
	'Z'-shaped Ag metamaterials	CPL	1.2–1.5	~0.55*	/	0.002	Yes	145
	Gra/Au antenna	CPL	4.0	~∞	93×10^{-9}	392 V/W	Yes	146
	Te nanosheets/ V-shaped grooves	CPL	0.4	107	290×10^{-6}	0.29 V/W	Yes	147
	InSe/Au metamaterial	CPL	0.5–1.1	1.6×10^4	320×10^{-6}	0.19	Yes	148

photoresponse via geometric SDM, with the photocurrent direction and magnitude strictly determined by the incident polarization angle. This allows a single element to distinguish between changes in light intensity and polarization rotation, enabling simultaneous analytical measurement of optical power and polarization in the mid-infrared, laying the foundation for compact, calibration-free multidimensional optical detection. Beyond non-centrosymmetric gold nanoantennas, our group developed a rotation-symmetry grating contact photodetector (RGCP) (Fig. 8(c, d))[157]. Employing a three-terminal architecture with triple rotational symmetry, the device produces two linearly independent bipolar photocurrents, enabling single-pixel analytical determination of incident power and polarization angle. To further enhance discrimination and flexibility, Wei et al. engineered the orientation of nanoantennas to customize the SDM matrix elements, enabling configurable polarity transitions and achieving a *PR* tunable from positive to negative infinity (Fig. 8(e))[158]. In contrast to these static designs, Li et al. proposed an electrically tunable $MoTe_2$ metasurface photodetector operating on the TDM principle, where polarization sensitivity can be continuously modulated via a gate voltage (Fig. 8(f))[159]. Geometrically engineered structures successfully resolve linear polarization while maintaining high responsivity. However, characterizing the full polarization state requires capturing chirality. This necessitates expanding the design space, as chiral responses are typically inaccessible in planar symmetric architectures.

Unlike material-based strategies, metasurfaces offer a distinct pathway for detecting CP by engineering the instrument matrix ***M***. By integrating artificial chirality, these architectures enable full Stokes vector resolution. Li et al. adopted a standard SDM architecture by integrating chiral plasmonic metasurfaces with graphene-silicon photodetectors, constructing four distinct superpixels that include chiral Z-shaped antennas for CP and anisotropic rectangular antennas for linear polarization (Fig. 9(a,b))[160]. This monolithic rank-4 architecture enables simultaneous measurement of intensity, polarization orientation, and ellipticity at 1550 nm, thereby replacing bulky commercial polarimeters. To address the scarcity of intrinsic chirality in the mid-infrared, Dai et al. developed a multi-port SDM polarimeter based on the PTE (Fig. 9(c,d))[161]. By spatially arranging chiral meta-atoms to induce polarization-dependent temperature gradients, the device maps the four Stokes parameters to unique combinations of photovoltages across three ports, enabling full polarization state retrieval without an external bias. Combining this with mathematical optimization further enhances detection performance. Deng et

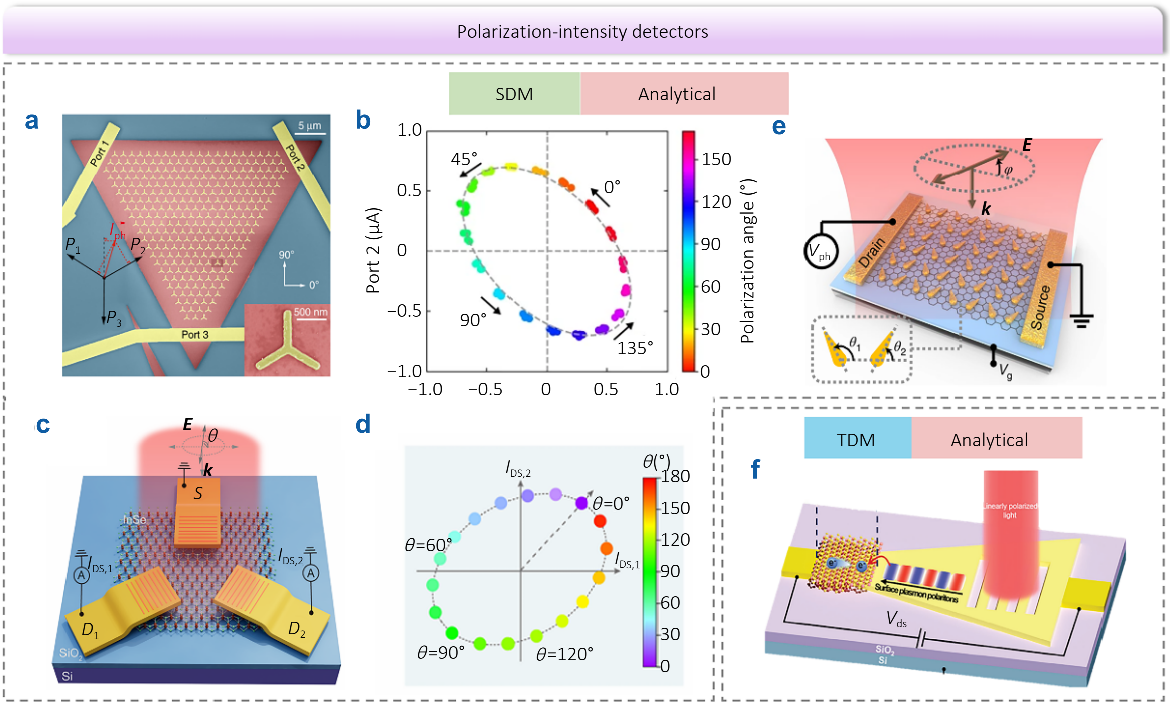

Fig. 8 | Metasurface-based polarization-intensity detectors. (a) Schematic illustrating the experimental setup of the Gr/BP/MoS_2/Gr vertical channel photodetector. (b) 2D plot of P_1 and P_2. By sweeping the polarization angle. (c) Schematic diagram of the full linear polarimetry photodetector. (d) 2D plots of the predicted $I_{DS,1}$ and $I_{DS,2}$ at different polarization angles. (e) Schematic of the nanoantenna-mediated semimetal photodetector. (f) Isotropic $MoTe_2$-based photodetector. Figure reproduced from: (a, b) ref.[156], Nature Publishing Group; (c, d) ref.[157], American Chemical Society; (e) ref.[158], Nature Publishing Group; (f) ref.[159], Wiley-VCH.

al. introduced the concept of "optoelectronic polarization eigenvectors". They optimized a metasurface on MoS_2 so that the four sub-pixels correspond to specific eigenvectors of the target Mueller matrix (Fig. 9(e, f))[162]. This approach explicitly minimizes the condition number of the instrument matrix as a primary design objective, maximizing robustness against experimental noise. Liu et al. proposed a metasurface photodetector for direct Stokes quantification (Fig. 9(g))[163]. The device employs channel-level decoupling to yield a responsivity matrix that approximates the identity matrix, thereby enabling each electrical output to correspond linearly to a specific Stokes parameter.

Following polarization detection, integrating wavelength sensing is critical. However, intrinsic high-mobility materials typically lack spectral discrimination due to their inherent broadband absorption. To extend polarization sensitivity into the spectral domain, researchers initially employed Resonance-based SDM strategies. By engineering meta-atoms to support specific electromagnetic modes—such as Fano or guided-mode resonances—metasurfaces effectively transform broadband detectors into devices with simultaneous wavelength and polarization selectivity. In the LWIR and terahertz ranges, Chen et al. designed a dual-band detector by integrating metamaterial microcavities with graphene. Each band responds to orthogonal polarization, yielding a diagonalized measurement matrix that enables simultaneous wavelength selection (2.52 THz and 3.11 THz) and polarization resolution on a single chip (Fig. 10(a))[164]. This demonstrated multicolor polarization imaging and on-chip dual-dimensional detection. Similarly, Xie et al. developed a graphene photodetector mediated by L-shaped plasmonic nanoantennas in the LWIR, leveraging narrow-band resonances for dual-mode spectral and polarization detection (Fig. 10(b))[165]. The device achieves ultra-high sensitivity to polarization angles (0.05°). It can detect gas absorption spectra by tuning the antenna resonance, enabling simultaneous polarization analysis and molecular spectral identification on a single chip. To reduce optical losses in metallic structures, Chu et al. proposed a vdWHs combining a MoS_2 dielectric grating with an InSe photosensitive flake (Fig. 10(c))[166]. Unlike metallic antennas, the MoS_2 grating supports low-loss guided-mode resonances, providing sharper spectral selectivity and high dichroic ratios in the NIR. Although these resonant structures perform well in narrow bands, continuous broadband detection remains challenging. In addition to analytical reconstruction, data-driven approaches have also been explored. For instance, Jiang et al. employed deep learning to classify discrete wavelength and polarization states based on metasurface outputs[167].

At the array level, for continuous spectral reconstruction, Wen et al. demonstrated a metasurface array-based

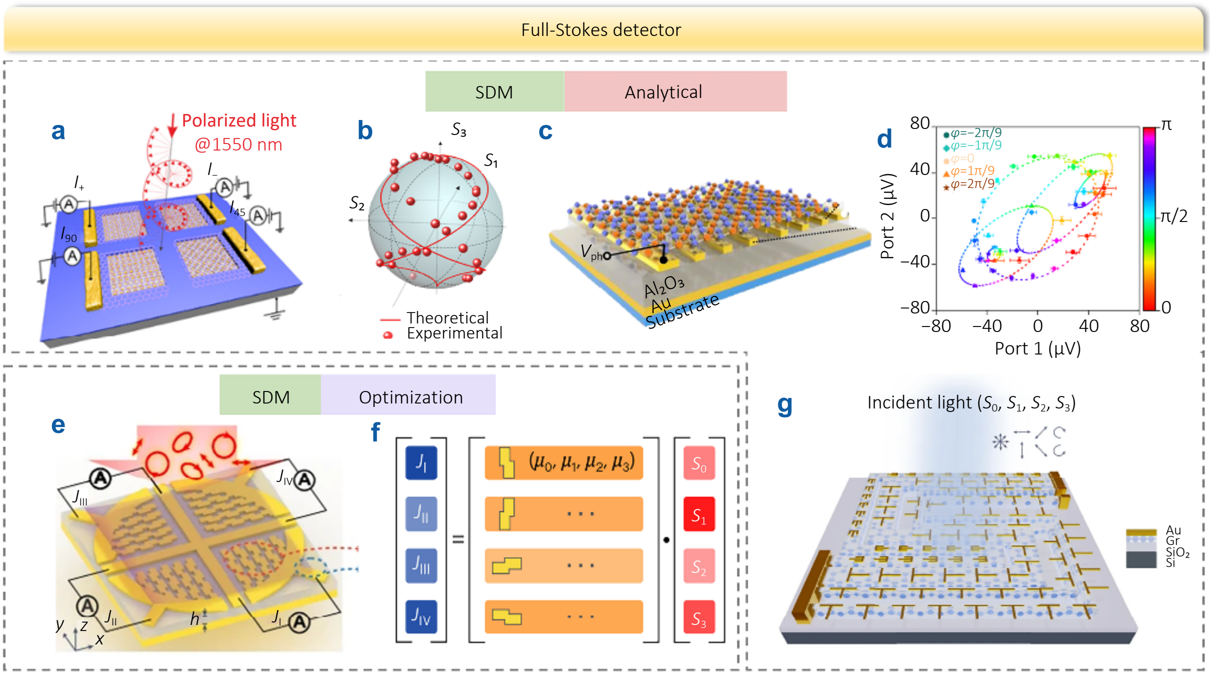

Fig. 9 | Metasurface-enhanced full-Stokes detectors. (a) Schematic diagram of the plasmonic polarimeter. (b) Measured SoPs on a Poincaré sphere from the four-pixel polarization analyzer with linearly polarized and elliptically polarized inputs. (c) Design principle of mid-IR photodetector based on resonance photo-thermoelectric response. (d) 2D plot of Port 1 and Port 2 under different azimuthal angle θ and ellipticity angle φ. (e) Device structure of the on-chip polarimeter. (f) Four-pixel photoelectric conversion matrix. (g) Direct Stokes photodetection using nanostructures atop graphene. Figure reproduced from: (a, b) ref.[160], American Chemical Society; (c, d) ref.[161], Nature Publishing Group; (e, f) ref.[162], Nature Publishing Group; (g) ref.[163], Nature Publishing Group.

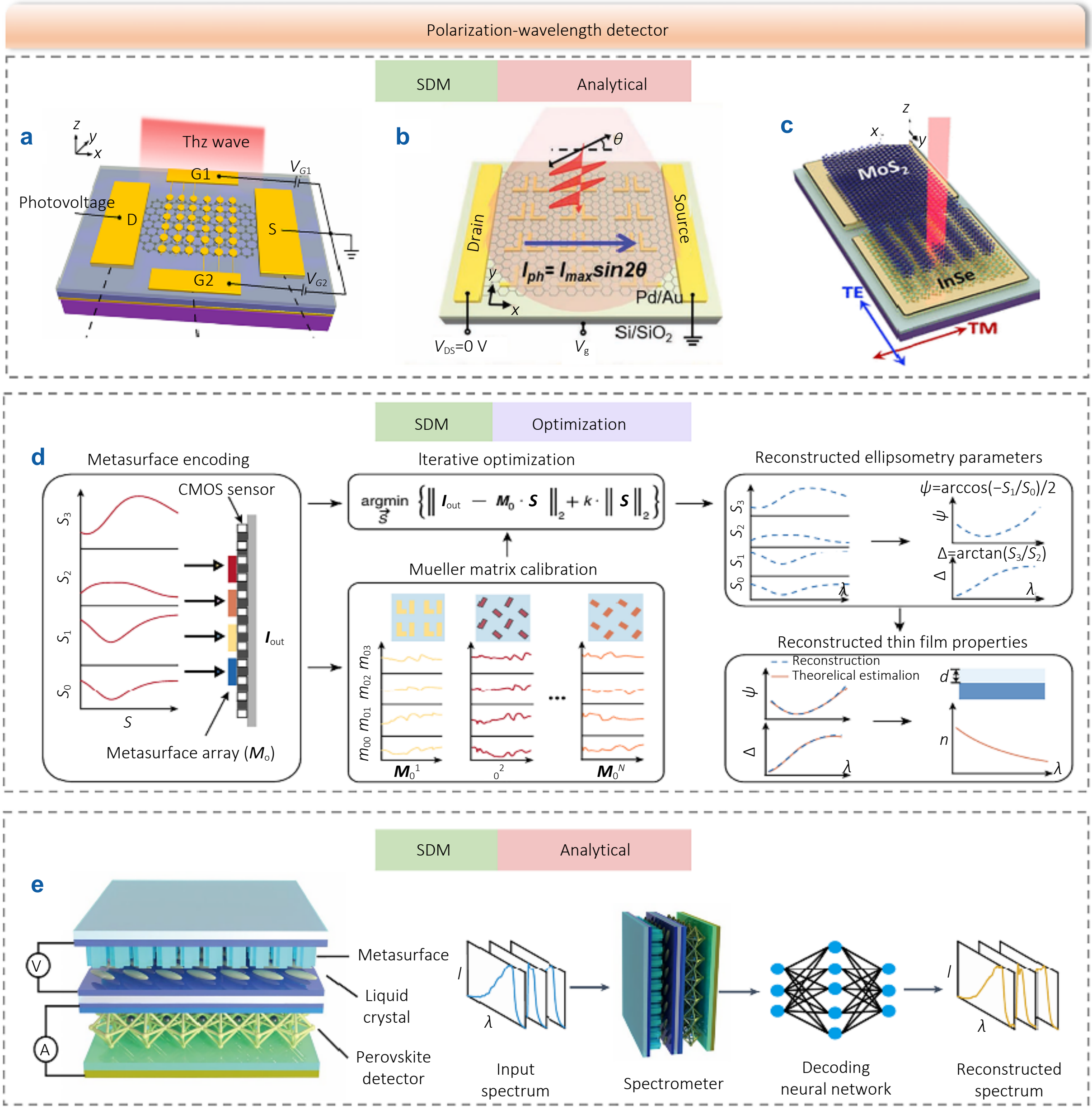

Fig. 10 | Metasurface-based polarization-wavelength detectors. (a) Schematic of the monolithic MM integrated graphene photodetector. (b) Measured polarization-dependent photoresponse. Illustration of the designed NMGPDs. (c) Device structure of MoS grating/InSe flake photodetector. (d) Working principle of the metasurface array-based single-shot spectroscopic ellipsometry. (e) Schematic and operation flow of a single compact meta-spectrometer. Figure reproduced from: (a) ref.[164], American Chemical Society; (b) ref.[165], Wiley-VCH; (c) ref.[166], American Chemical Society; (d) ref.[168], Nature Publishing Group; (e) ref.[170], Nature Publishing Group.

spectroscopic ellipsometer (Fig. 10(d))[168]. Unlike single-point resonance, this SDM architecture generates a diverse set of spectral response functions, enabling the retrieval of full Stokes spectra via iterative optimization algorithms. He et al. employed quasi-bound states in the continuum (quasi-BIC) metasurfaces for high-Q spectro-polarimetric detection, where quasi-BIC modes provide superior spectral resolution and enable high-dimensional data reconstruction through spatial multiplexin[169]. Furthermore, Cai et al. extended detection to the angular domain, developing a compact angle-resolved metasurface spectrometer (Fig. 10(e))[170]. By integrating a tunable metasurface array with a metalens, the device resolves both spectral and incident-angle information, achieving on-chip analytical angle-resolved spectral imaging. These studies demonstrate the potential of metasurfaces to integrate spectral, spatial, and angular information into a single platform for multidimensional optical measurement. In summary, metasurfaces leverage resonant mechanisms to transform broadband photodetectors into wavelength- and polarization-selective devices. Ranging from monolithic integration to intelligent array reconstruction, this approach enables compact, multidimensional optical analysis without bulky optical components.

Although array-level integration for joint polarization–wavelength detection has advanced, capturing light fields with arbitrarily mixed polarization, intensity, and spectral information in a single measurement remains highly challenging. To address this challenge of acquiring high-dimensional information with minimal hardware, Fan et al. proposed a dispersion-assisted SDM strategy coupled with deep learning decoding (Fig. 11(a,b))[171]. They utilized simple thin-film interfaces possessing both spatial and frequency dispersion to map multidimensional optical information into the wavevector domain. By encoding polarization and spectral responses into specific incident and azimuth angles, the device converts high-dimensional signatures into a spatial intensity distribution, which is then decoded by a deep residual network. This approach enables simultaneous reconstruction of intensity, full-Stokes polarization vectors, and broadband spectra (400–900 nm), demonstrating that a combination of "structure and algorithm" can replace complex hardware. While this demonstrates the potential of "structure plus algorithm" to replace complex hardware, it is critical to recognize that the retrieval process is ill-posed due to the limited physical degrees of freedom of the planar interface. Consequently, the high-dimensional reconstruction relies heavily on algorithmic priors, which may impose generalization constraints when the target light field deviates statistically from the training dataset.

The ultimate goal of photodetection is to reconstruct the complete optical field tensor, including OAM. Although intrinsic-material-based approaches, such as the OPGE in Weyl semimetals or graphene, have demonstrated direct electrical readout of OAM, these methods are fundamentally limited by the material's crystal structure, resulting in low responsivity and weak light-matter interaction. Metasurfaces, with their powerful light-field manipulation capabilities, can overcome these physical limitations by converting free-space optical angular momentum into locally readable modes or spatial patterns. For example, Dai et al. implemented a geometric SDM architecture integrating a spin-Hall surface plasmon polariton (SPP) coupler with a $PdSe_2$ thermoelectric detector (Fig. 11(c, d))[172]. Unlike OPGE approaches that rely on specific band structures, this device spatially sorts and focuses light carrying different SAM and OAM using a micro-nano grating structure. The PTE directly maps angular-momentum modes to distinct voltage outputs, enabling reliable detection of vortex-beam chirality and topological charge. In the terahertz regime, Zhang et al. innovatively used a dispersion-driven OAM multiplication mechanism with deep learning decoding to encode incident frequency and polarization information into complex polaritonic vortex patterns via a metasurface (Fig. 11(e, f))[173]. Combined with deep learning algorithms, this system accurately decouples and reconstructs intensity, full-Stokes polarization vectors, and ultra-broadband frequency information (0.3–1.1 THz) from multiplexed OAM modes. It is noteworthy, however, that mapping continuous parameter spaces onto a finite set of discrete OAM modes inherently involves information compression. Consequently, the decoding fidelity relies heavily on signal sparsity and the neural network's priors to resolve the non-injective mapping, which may limit performance for dense broadband signals due to the mathematical ill-posedness. These studies demonstrate that metasurface engineering can effectively overcome the intrinsic limitations of material-based OAM response mechanisms, opening new avenues for on-chip, high-dimensional, and multi-physical-quantity photodetection.

In summary, Section 5 has systematically explored photodetection strategies enabled by metasurface engineering. Progress ranges from the rigorous optimization of single-dimensional metrics—such as responsivity and polarization selectivity via subwavelength geometric design—to the integrated detection of high-dimensional information, including full-Stokes vectors and OAM, achieved through spatial dispersion and computational reconstruction. These structural approaches effectively surmount the physical constraints of natural materials, enabling the sensing of complex, multidimensional optical fields within compact devices.

To rigorously benchmark the two dominant technological paradigms discussed in Section 4 and 5, Fig. 12 provides a comprehensive comparative analysis. The radar chart in Fig. 12(a) shows a clear trade-off among performance metrics: while intrinsic materials (purple region) excel in fundamental optoelectronic properties such as responsivity and spectral bandwidth due to their efficient carrier generation and transport, they are often constrained by crystal symmetry. In contrast, metasurface-integrated systems (pink region) significantly outperform in polarization ratio and design freedom, utilizing extrinsic structural engineering to break physical symmetry limits. This technological divergence is further quantified in Fig. 12(b), which maps the information dimensionality (N) against the operating wavelength. A clear stratification is observed: low-dimensional detection ($N \leq 2$) is largely populated by intrinsic material architectures. However, the transition to the high-dimensional frontier ($N \geq 3$) is predominantly enabled by metasurface-enhanced designs. This distribution underscores a critical conclusion: while intrinsic materials constitute the necessary physical foundation for high-sensitivity photon-to-electron conversion, metasurface engineering serves as the essential modality for decoding complex, high-dimensional optical field tensors.

6 Silicon-based integrated photodetectors for on-chip perception

Individual photodetection units, whether optimized through intrinsic material symmetry (Section 4) or through localized

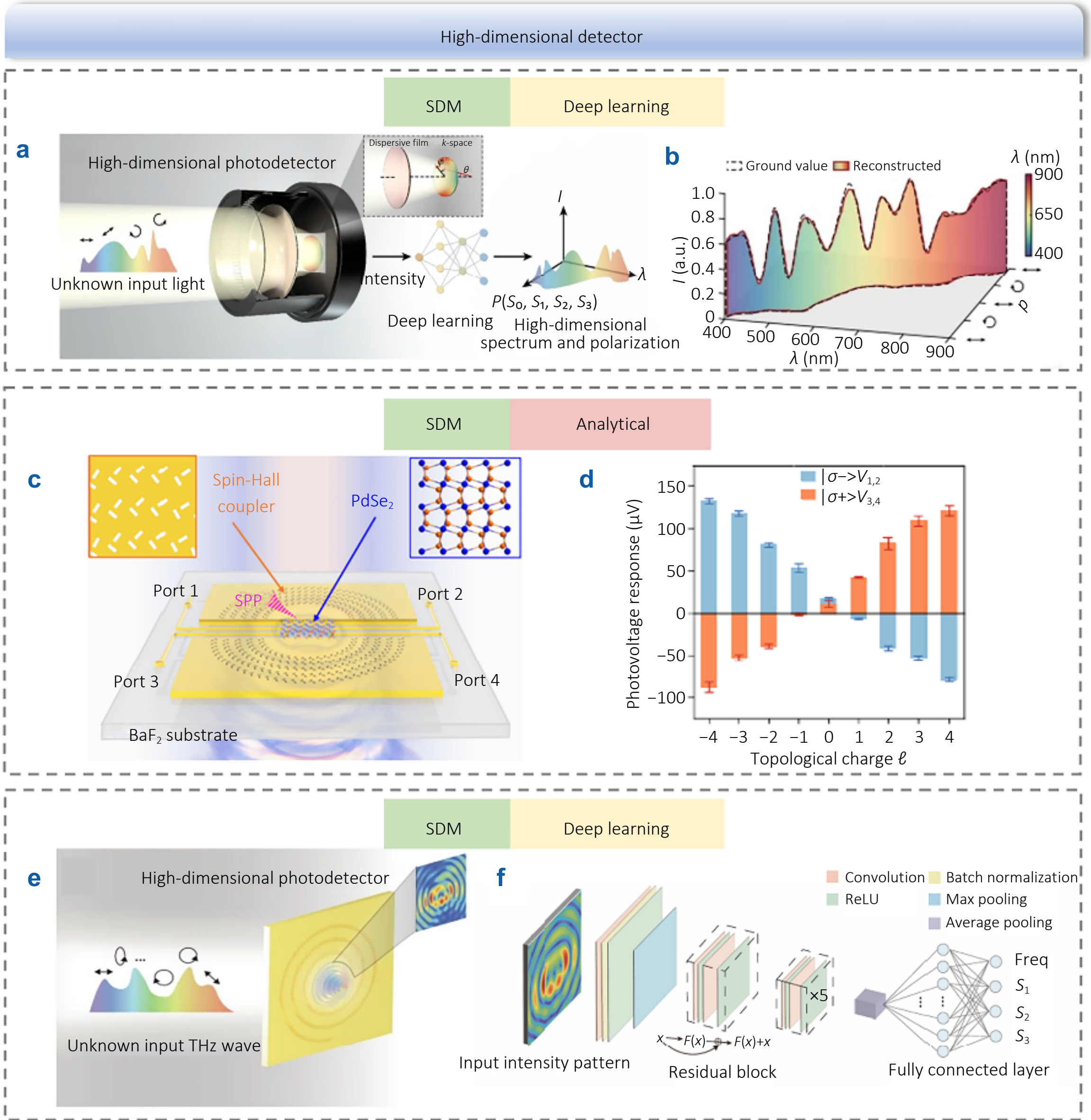

Fig. 11 | Metasurface-based high-dimensional detector. (a) Schematic of a spectral-polarization photodetector. (b) Complex spectral-full Stokes detection reconstruction effect. (c, b) Design principles of our on-chip photodetector for vortex light. (e) Ultra-broadband terahertz high-dimensional photodetector. (f) Architecture of the employed neural network for high-dimensional detection, the output layer is a vector indicating Stokes parameters and wavelength information. Figure reproduced from: (a, b) ref.[171], Nature Publishing Group; (c, d) ref.[172], Nature Publishing Group; (e, f) ref.[173], Nature Publishing Group.

metasurface engineering (Section 5), have demonstrated remarkable potential for capturing multidimensional optical information. However, transforming these discrete physical phenomena into practical, high-throughput sensing applications necessitates a transition from standalone devices to system-level architectures. Silicon photonics, leveraging its mature, CMOS-compatible fabrication infrastructure, serves as the indispensable enabler of this evolution[174–177]. The high-index contrast of the SOI platform enables the high-density integration of complex optical paths—such as interferometers, resonators, and disordered waveguides—within a compact footprint. This synergy allows for the large-scale deployment of sensor arrays and provides the necessary systemic infrastructure—such as robust packaging and efficient light-coupling—to transform individual sensing mechanisms into a unified, functional chip-scale system[178].

Beyond physical integration, the true paradigm shift offered by the silicon photonic platform is the realization of Intellectualization through the fusion of perception and

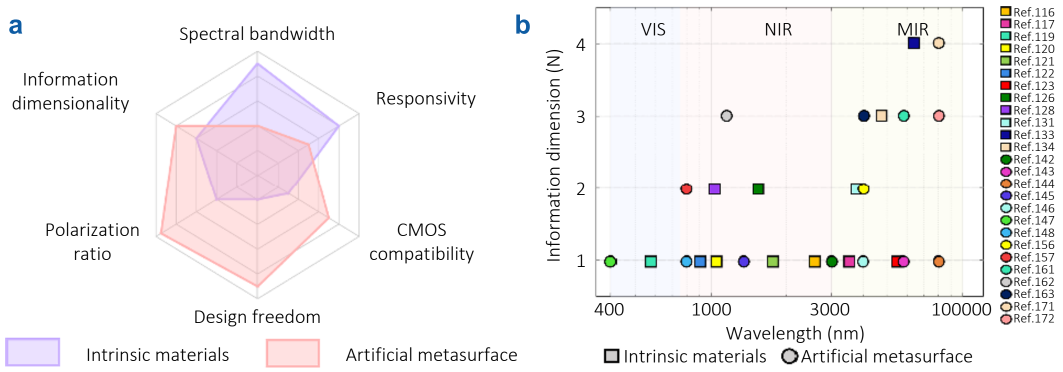

Fig. 12 | Performance comparison of photodetectors with different architectures. (a) Comparative radar chart: a multi-axis comparison of six key figures of merit between intrinsic material (purple region) and metasurfac systems (pink region). (b) Operational landscape mapping information dimensionality (*N*) as a function of operating wavelength. The distribution of intrinsic materials (squares) and metasurface systems (circles) illustrates the technological transition from low-dimensional detectionto (*N*=1) high-dimensional sensing (*N*=4) enabled.

computation. While material and metasurface engineering primarily focus on maximizing the "raw" optoelectronic response, silicon-based architectures enable seamless coupling of light-field sensitizers with on-chip signal-processing units. By implementing architectures such as photonic neuromorphic processors or in-sensor computing nodes, the silicon platform can perform complex information decoupling—such as full-Stokes polarization reconstruction and spectral analysis—directly in the optical domain or via integrated electronic feedback. This synergy transforms the photodetector from a passive energy converter into an intelligent perception system capable of real-time, high-level feature extraction. Consequently, this section shifts the focus to system integration, investigating how inverse design, programmable photonic circuits, and in-sensor computing architectures can integrate these high-performance units organically, thereby advancing photodetection toward intelligent on-chip perception.

On-chip multidimensional fusion requires extreme miniaturization of functional components to support high-density integration. Traditional designs are often bulky, limiting the number of spectral or polarization channels. To address this via the PNoC encoding strategy, Piggott et al. proposed inverse-designed dielectric structures, demonstrating an ultracompact (2.8 μm×2.8 μm) wavelength demultiplexer capable of separating broadband light into distinct spectral channels with low insertion loss (Fig.13(a))[179]. This topology-optimized approach offers a general solution for high-density spectral interfaces required for multidimensional analysis. Beyond static spectral separation, dynamic handling of OAM is critical for high-dimensional sensing. To handle structured light with reconfigurable flexibility, Bütow et al. developed a programmable PNoC photonic processor composed of a mesh of MZIs (Fig. 13(b))[180]. This architecture enables on-chip reconfigurable sorting and demultiplexing of structured light beams with different OAM modes, providing a flexible interface for analytical spatial-mode processing. To further reduce latency between detection and processing, Liu et al. implemented photonic in-sensor computing on a mid-infrared silicon waveguide platform (Fig. 13(c))[181]. By integrating responsivity-tunable graphene photodetectors onto waveguides, they performed weighting operations via bias modulation, thereby embedding deep learning neural network computation within the sensing front end.

As the number of target dimensions increases, deterministic design strategies face channel-scaling bottlenecks. Disordered photonics offers a breakthrough by leveraging complex scattering as a high-dimensional encoding mechanism. Breaking the scaling bottleneck via the disordered SDM paradigm, Zhu et al. used a disordered medium to map four-dimensional optical information into unique speckle patterns (Fig. 13(d))[182]. Combined with multi-task learning, this system enables single-shot recognition of intensity, polarization, OAM, and wavelength, overcoming the physical channel limitations of traditional spectrometers. Building on this concept, Gu et al. proposed a disordered-guided photonic chip that integrates a scattering region with a waveguide collection area (Fig. 13(e))[183]. This design efficiently encodes high-dimensional inputs into multi-channel intensities, allowing high-accuracy reconstruction of mixed full-Stokes polarization and broadband spectra. However, utilizing disordered photonics trades physical determinism for algorithmic complexity. The system's reliance on strict speckle mapping renders it vulnerable to environmental perturbations (e.g., temperature drift), creating challenges for long-term robustness and recalibration compared to deterministic designs. Integrating these advances, Gu et al. demonstrated a fully integrated multidimensional optical sensing system that unifies sensing and computation on a single chip (Fig. 13(f))[184]. Realizing the merging of PNoC encoding with optical deep learning decoding, the device combines an inverse-designed light-field sensitizer with a photonic neural network (ONN: a computing architecture

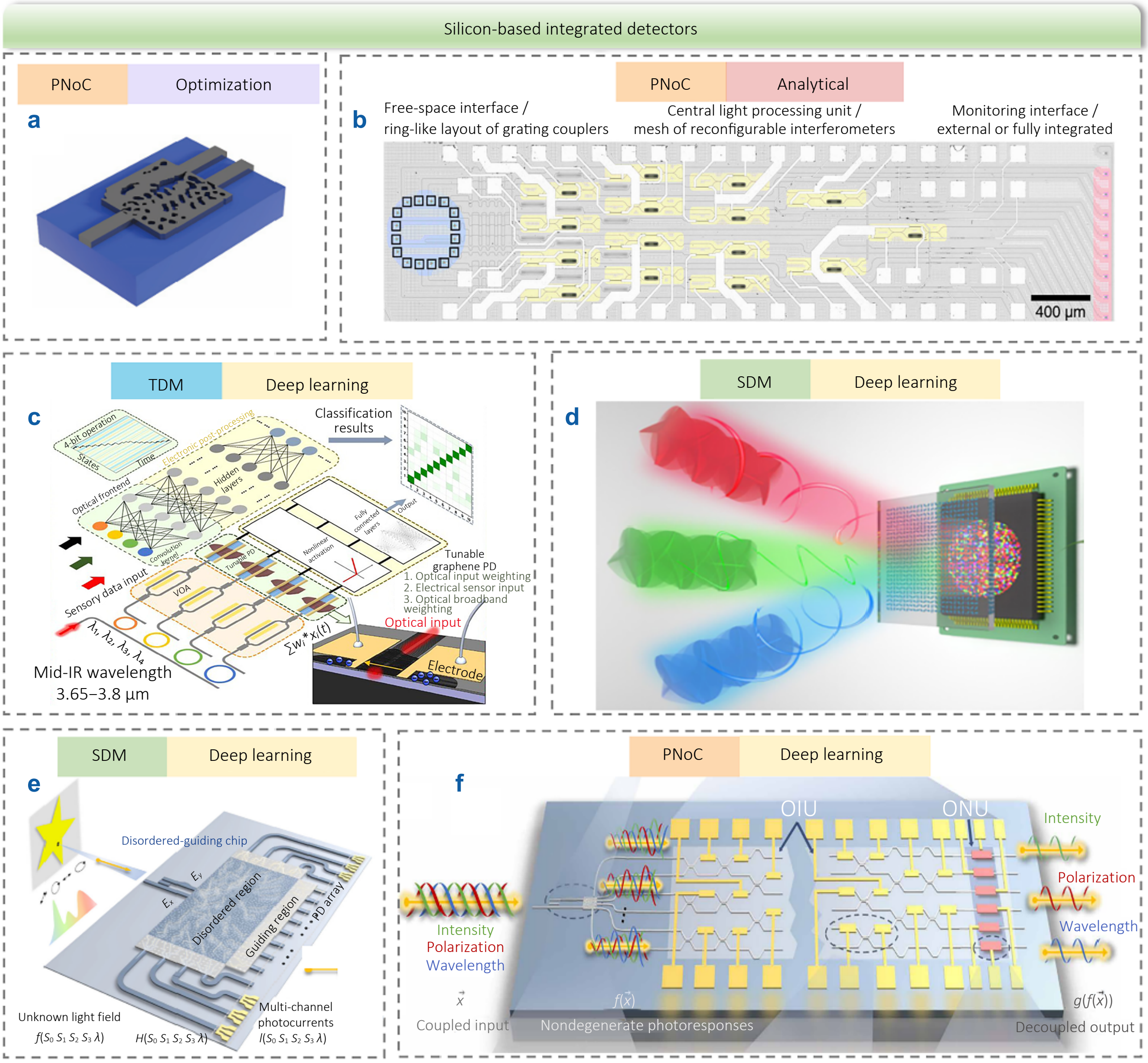

Fig. 13 | Silicon-based integrated detectors for on-chip perception. (a) The compact wavelength demultiplexer designed by the inverse design algorithm. (b) Utilized a photonic integrated processor. (c) Schematics of the proposed waveguide-integrated MIR optoelectronic processing unit. (d) Schematic of integrated four-dimensional light field sensors via disordered nematic liquid crystal (NLC) medium, imaging chip, and deep learning. (e) The principle of a high-dimensional detection and imaging system. (f) All-integrated multidimensional optical sensing with a photonic neuromorphic processor. Figure reproduced from: (a) ref.[179], Nature Publishing Group; (b) ref.[180], Nature Publishing Group; (c) ref.[181], American Chemical Society; (d) ref.[182], Springer Nature; (e) ref.[183], Nature Publishing Group; (f) ref.[184], American Association for the Advancement of Science.

that utilizes optical components to perform neural network operations at the speed of light) processor. The sensitizer projects multidimensional incident light (intensity, polarization, and wavelength) into parallel waveguide channels, which are then processed directly by the reconfigurable ONN to produce decoupled classification results. This fully on-chip architecture eliminates optical-to-electrical conversion latency and offline digital processing, achieving 91% accuracy and an ultrafast processing speed of 100 GB/s.

In summary, Section 6 demonstrates the system-level integration and intelligence of photodetection on silicon platforms. Techniques such as topology optimization and disordered photonics effectively resolve challenges related to device miniaturization and channel scaling. Furthermore, embedding ONNs directly in the sensing front end eliminates data transmission latency. This "sensing-computing" paradigm transforms the optoelectronic chip from a simple signal converter into a high-speed, intelligent perception system, thereby charting a clear course for next-generation optoelectronic architectures.

Finally, to summarize the current landscape of high-dimensional perception, Table 2 catalogues the performance of representative multidimensional photodetectors reviewed herein. By categorizing devices based on their multiplexing strategies and detectable dimensions (intensity, polarization, spectrum, OAM), this comparison provides a clear reference for the capabilities of different architectures. It becomes evident that while individual devices have achieved remarkable multi-parameter decoupling, the future trend lies in scaling these units into fully integrated systems to further enhance information capacity.

7 Conclusion and prospect

This review systematically traces the evolution of multidimensional photodetection through the lens of a hardware-software synergistic framework, from intrinsic material mechanisms to metasurface-enhanced architectures and, finally, to system-level integration. The discussion commenced by exploring how the unique band structures and crystal symmetries of low-dimensional materials provide the physical basis for responding to single-dimensional optical fields. While these intrinsic properties offer a starting point, we demonstrated that metasurfaces can significantly amplify these capabilities through subwavelength structural engineering, enabling precise decoupling of entangled parameters such as intensity, polarization, and spectrum. Furthermore, the exploration of silicon photonic integration highlights a promising pathway toward realizing fully on-chip, intelligent perception systems.

Despite these remarkable advancements, several critical bottlenecks must be overcome before high-dimensional photodetectors can be widely deployed in practical applications. A primary hurdle lies in the wafer-scale synthesis and homogeneity of high-quality optoelectronic materials. Unlike mature silicon technologies, emerging materials such as twisted heterostructures and perovskites often exhibit high defect densities and grain boundaries during large-area growth, leading to significant pixel-to-pixel performance variations that degrade imaging accuracy. Furthermore, efficient carrier extraction is often impeded by Fermi-level pinning at metal-semiconductor interfaces, resulting in high Schottky barriers and contact resistance that limit device speed. Additionally, as detectors evolve to capture multidimensional information simultaneously, the exponential increase in data volume poses a challenge for current serial readout architectures, necessitating the co-design of high-bandwidth parallel readout integrated circuits and on-chip compression algorithms.

Ultimately, realizing the full potential of these multidimensional detectors requires overcoming this scalability bottleneck. While transfer-based methods have enabled rapid prototyping, future mass production will likely rely on a hybrid evolution of manufacturing technologies. Promisingly, recent breakthroughs have demonstrated the feasibility of wafer-scale direct growth. For instance, seeded solid-phase epitaxy has been successfully employed to synthesize wafer-scale 2H-$MoTe_2$ single-crystal arrays, offering a robust pathway to circumvent the transfer bottleneck. Simultaneously, advanced automated transfer strategies are bridging the gap towards fab-line compatibility, as extensively reviewed by Ago et al., who highlighted that emerging 'clean transfer' techniques are now meeting the stringent yield requirements of industrial integration. These developments suggest that the integration of high-performance low-dimensional materials with silicon photonics is steadily moving from fundamental research toward industrial reality.

Table 2 | The performance of multi-dimensional detector.

Materials	Strategy	Wavelength (μm)	Response time (s)	Responsivity (A/W)	Intensity	Spectral	Polarization	OAM	Ref.
$PdSe_2/MoS_2$	TDM	0.52–1.55	$7–12\times10^{-6}$	0.122	Yes	No	AoLP and DoLP	No	128
BP	SDM	1.55	800×10^{-9}	$\sim0.5\times10^{-3}$	Yes	No	LP or CPL	No	126
Twisted bilayer graphene	TDM	5.0–7.7	$<50\times10^{-6}$	0.7×10^{-3}	Yes	Yes	Full-Stokes	No	133
Bp\\MoS_2\\Asp	TDM	2–5.5	500×10^{-9}	857×10^{-3}	No	Yes	LP	No	131
Double twisted BP	SDM	3.7–5.7	21×10^{-6}	50×10^{-3}	Yes	Yes	LP	No	134
Graphene/Au antennas	SDM	4	100×10^{-6}	16.6×10^{-3}	Yes	No	LP	No	156
InSe/Au metamaterial	SDM	0.633, 0.78, 0.98	380×10^{-6}	530×10^{-3}	Yes	No	LP	No	157
$PdSe_2$/Au metamaterial	SDM	4.5–7.0	76×10^{-6}	3.6 V/W	Yes	No	Full-Stokes	No	161
MoS_2/Au metamaterial	SDM	1.15	14×10^{-6}	4.76×10^{-3}	Yes	No	Full-Stokes	No	162
Graphene/Au metamaterial	SDM	4	675×10^{-9}	116.7 V/W	Yes	No	Full-Stokes	No	163
$PdSe_2$/Au metamaterial	SDM	8	69×10^{-6}	$j \times \pm0.2$ mV/W	No	No	CPL	Yes	172
Lens-film-CMOS	SDM	0.4–0.9	N.A.	N.A.	Yes	Yes	Full-Stokes	No	171
Programmable MZI mesh	SDM	1.57	N.A.	N.A.	Yes	No	No	Yes	180

Looking forward, the field is poised for transformative leaps driven by the convergence of active photonics and intelligent computing. Future research will likely shift from static optical filtering to dynamically reconfigurable perception, incorporating active metasurfaces to create programmable photodetectors that can adaptively switch between hyperspectral imaging and polarization encryption. Moreover, deep learning algorithms will become a standard component of the detection pipeline. By training neural networks to decode the complex response matrices of physical structures, detectors can achieve super-resolution and high-fidelity reconstruction that transcends the physical limits of hardware alone. Ultimately, this synergy among advanced materials, innovative structural designs, and intelligent computation will transform photodetectors from simple signal converters into smart nodes capable of comprehensive light-field perception.

References

1. Morteza Najarian A, Vafaie M, Chen B et al. Photophysical properties of materials for high-speed photodetection. *Nat Rev Phys* **6**, 219–230 (2024).
2. Zhong F, Chen YZ, Yan PD et al. Multidimensional photodetection of light fields based on metasurfaces or two-dimensional materials. *Appl Phys Lett* **124**, 140501 (2024).
3. Hu YX, Gao ZL, Luo ZT et al. Next-generation image sensors based on low-dimensional semiconductor materials. *Adv Mater* **37**, 2501123 (2025).
4. He C, He HH, Chang JT et al. Polarisation optics for biomedical and clinical applications: a review. *Light Sci Appl* **10**, 194 (2021).
5. Zou KH, Pang K, Song H et al. High-capacity free-space optical communications using wavelength- and mode-division-multiplexing in the mid-infrared region. *Nat Commun* **13**, 7662 (2022).
6. Chen MF, Chen XQ, Wu ZQ et al. An ultrasensitive Bi_2O_2Se/In_2S_3 photodetector with low detection limit and fast response toward high-precision unmanned driving. *ACS Nano* **18**, 27579–27589 (2024).
7. Liu X, Deng CY, Wei H et al. High-sensitive uncooled mid-wave infrared photodetector based on $PtSe_2/MoTe_2$ heterojunction with fast speed. *Adv Funct Mater* **35**, 2423102 (2025).
8. Yoshioka K, Wakamura T, Hashisaka M et al. Ultrafast intrinsic optical-to-electrical conversion dynamics in a graphene photodetector. *Nat Photonics* **16**, 718–723 (2022).
9. Jiang H, Wei JX, Sun FY et al. Enhanced photogating effect in graphene photodetectors *via* potential fluctuation engineering. *ACS Nano* **16**, 4458–4466 (2022).
10. Ouyang X, Xu Y, Xian MC et al. Synthetic helical dichroism for six-dimensional optical orbital angular momentum multiplexing. *Nat Photonics* **15**, 901–907 (2021).
11. He C, Shen YJ, Forbes A. Towards higher-dimensional structured light. *Light Sci Appl* **11**, 205 (2022).
12. Forbes A, de Oliveira M, Dennis MR. Structured light. *Nat Photonics* **15**, 253–262 (2021).
13. Li SX, Feng JC, An Y et al. Flexible, self-powered, and polarization-sensitive photodetector based on perovskite lateral heterojunction microwire arrays. *Photonics Res* **11**, 2231–2241 (2023).
14. Fang WZ, Liu CB, Zhu ZX et al. Bioinspired single-shot polarization photodetector based on four-directional grating arrays capped perovskite single-crystal thin film. *Sci Adv* **10**, eadr5375 (2024).
15. Li QT, van de Groep J, Wang YF et al. Transparent multispectral photodetectors mimicking the human visual system. *Nat Commun* **10**, 4982 (2019).
16. Zhao YJ, Yin X, Li PW et al. Multifunctional perovskite photodetectors: from molecular-scale crystal structure design to micro/nano-scale morphology manipulation. *Nano-Micro Lett* **15**, 187 (2023).
17. Shen DZ, Yang HB, Patel T et al. Gate-tunable multiband van der Waals photodetector and polarization sensor. *ACS Nano* **18**, 11193–11199 (2024).
18. El Hamdani S, Benamar N, Younis M. Pedestrian support in intelligent transportation systems: challenges, solutions and open issues. *Transp Res Part C Emerg Technol* **121**, 102856 (2020).
19. Meiring, G. A., Myburgh, H. C. A review of intelligent driving style analysis systems and related artificial intelligence algorithms. *Sensors* **15**, 30653–30682 (2015).
20. Qiu XD, Guo HX, Chen LX. Remote transport of high-dimensional orbital angular momentum states and ghost images via spatial-mode-engineered frequency conversion. *Nat Commun* **14**, 8244 (2023).
21. Rosati M, Solana A. Joint-detection learning for optical communication at the quantum limit. *Opt Quantum* **2**, 390–396 (2024).
22. Nunes-Pereira EJ, Peixoto H, Teixeira J et al. Polarization-coded material classification in automotive LIDAR aiming at safer autonomous driving implementations. *Appl Opt* **59**, 2530–2540 (2020).
23. Liu MX, Wei JX, Qi LJ et al. Photogating-assisted tunneling boosts the responsivity and speed of heterogeneous WSe_2/Ta_2NiSe_5 photodetectors. *Nat Commun* **15**, 141 (2024).
24. Zhang YX, Zhang S, Wu H et al. Miniature computational spectrometer with a plasmonic nanoparticles-in-cavity microfilter array. *Nat Commun* **15**, 3807 (2024).
25. Xue Q, Yang Y, Ma WK et al. Advances in miniaturized computational spectrometers. *Adv Sci* **11**, 2404448 (2024).
26. Peinado A, Turpin A, Lizana A et al. Conical refraction as a tool for polarization metrology. *Opt Lett* **38**, 4100–4103 (2013).
27. Wu Q, Gao L, Cao YL et al. Single-shot measurement of wavelength-resolved state of polarization dynamics in ultrafast lasers using dispersed division-of-amplitude. *Photonics Res* **11**, 35–43 (2023).
28. Yang ZY, Albrow-Owen T, Cai WW et al. Miniaturization of optical spectrometers. *Science* **371**, eabe0722 (2021).
29. Craven-Jones J, Kudenov MW, Stapelbroek MG et al. Infrared hyperspectral imaging polarimeter using birefringent prisms. *Appl Opt* **50**, 1170–1185 (2011).
30. Qi J, He C, Elson DS. Real time complete Stokes polarimetric imager based on a linear polarizer array camera for tissue polarimetric imaging. *Biomed Opt Express* **8**, 4933–4946 (2017).
31. Wu SQ, Chen Y, Wang XD et al. Ultra-sensitive polarization-resolved black phosphorus homojunction photodetector defined by ferroelectric domains. *Nat Commun* **13**, 3198 (2022).
32. Tan T, Jiang XT, Wang C et al. 2D material optoelectronics for information functional device applications: status and challenges. *Adv Sci* **7**, 2000058 (2020).
33. Novoselov KS, Mishchenko A, Carvalho A et al. 2D materials and van der Waals heterostructures. *Science* **353**, aac9439 (2016).
34. Zeng SF, Tang ZW, Liu CS et al. Electronics based on two-dimensional materials: status and outlook. *Nano Res* **14**, 1752–1767 (2021).

35. Wang F, Zhang T, Xie RZ et al. Next-generation photodetectors beyond van der Waals junctions. *Adv Mater* **36**, 2301197 (2024).
36. Wang XJ, Van Mechelen T, Bharadwaj S et al. Exploiting universal nonlocal dispersion in optically active materials for spectro-polarimetric computational imaging. *eLight* **4**, 22 (2024).
37. Dushaq G, Serunjogi S, Tamalampudi SR et al. Electro-optic tuning in composite silicon photonics based on ferroionic 2D materials. *Light Sci Appl* **13**, 92 (2024).
38. Cheng Z, Cao R, Wei KK et al. 2D materials enabled next-generation integrated optoelectronics: from fabrication to applications. *Adv Sci* **8**, 2003834 (2021).
39. Xia FN, Mueller T, Lin YM et al. Ultrafast graphene photodetector. *Nat Nanotechnol* **4**, 839–843 (2009).
40. Du SC, Lu W, Ali A et al. A broadband fluorographene photodetector. *Adv Mater* **29**, 1700463 (2017).
41. Kang P, Wang MC, Knapp PM et al. Crumpled graphene photodetector with enhanced, strain-tunable, and wavelength-selective photoresponsivity. *Adv Mater* **28**, 4639–4645 (2016).
42. Koepfli SM, Baumann M, Koyaz Y et al. Metamaterial graphene photodetector with bandwidth exceeding 500 gigahertz. *Science* **380**, 1169–1174 (2023).
43. Taffelli A, Dirè S, Quaranta A et al. MoS_2 based photodetectors: a review. *Sensors* **21**, 2758 (2021).
44. Gherabli R, Indukuri SRKC, Zektzer R et al. $MoSe_2/WS_2$ heterojunction photodiode integrated with a silicon nitride waveguide for near infrared light detection with high responsivity. *Light Sci Appl* **12**, 60 (2023).
45. Wang FK, Hu FC, Dai MJ et al. A two-dimensional mid-infrared optoelectronic retina enabling simultaneous perception and encoding. *Nat Commun* **14**, 1938 (2023).
46. Fu ZY, Han JY, Wei LJ et al. Polarization-sensitive self-powered photodetector based on anisotropic/isotropic $ReS_2/SnSe_2$ van der Waals heterojunction. *Adv Opt Mater* **12**, 2401306 (2024).
47. Wu WL, Liu ZY, Qiu ZC et al. An ultrasensitive $ReSe_2/WSe_2$ heterojunction photodetector enabled by gate modulation and its development in polarization state identification. *Adv Opt Mater* **12**, 2301410 (2024).
48. Jiao HX, Wang XD, Chen Y et al. HgCdTe/black phosphorus van der Waals heterojunction for high-performance polarization-sensitive midwave infrared photodetector. *Sci Adv* **8**, eabn1811 (2022).
49. Zhang SK, Huang XN, Chen Y et al. Black arsenic phosphorus mid-wave infrared barrier detector with high detectivity at room temperature. *Adv Mater* **36**, 2313134 (2024).
50. Tang F, Wu JJ, Albrow-Owen T et al. Metasurface spectrometers beyond resolution-sensitivity constraints. *Sci Adv* **10**, eadr7155 (2024).
51. Liu JJ, Yang XX, Xu QL et al. Unraveling the efficiency losses and improving methods in quantum dot-based infrared up-conversion photodetectors. *Opto-Electron Sci* **3**, 230029 (2024).
52. Hu JK, Wu JY, Jin D et al. Integrated photonic polarizers with 2D reduced graphene oxide. *Opto-Electron Sci* **4**, 240032 (2025).
53. Yao ZY, Liu SY, Wang YC et al. Integrated lithium niobate photonics for sub-ångström snapshot spectroscopy. *Nature* **646**, 567–575 (2025).
54. Han JY, Fu ZY, Wei JX et al. 2D materials-based next-generation multidimensional photodetectors. *Light Sci Appl* **14**, 362 (2025).
55. Sun SW, Wei JX, Wang JY et al. Polarization-sensitive photoelectric conversion. *Chem Rev* **126**, 1470–1533 (2026).
56. Zhang PY, Sun YH, Sun JC et al. Progress in 2D material-based infrared photodetectors for intelligent vision applications. *Adv Funct Mater* **35**, 2502072 (2025).
57. Yang J, Wang W, Bao CX et al. Toward practical applications of perovskite photodetectors: advantages and challenges. *Matter* **8**, 102207 (2025).
58. Zhao XR, Lou TM, Peng Y et al. Metasurface-based photodetectors: pursuing superior performance and multifunctionality. *ACS Photonics* **12**, 4096–4118 (2025).
59. Xin W, Zhong WH, Shi YJ et al. Low-dimensional-materials-based photodetectors for next-generation polarized detection and imaging. *Adv Mater* **36**, 2306772 (2024).
60. Chai Y. Silicon photodiodes that multiply. *Nat Electron* **5**, 483–484 (2022).
61. Johnston MB. Optoelectronics: fast silicon photodiodes. *Nat Photonics* **11**, 268–269 (2017).
62. Geum DM, Lim J, Jang J et al. Highly-efficient (>70%) and Wide-spectral (400-1700 nm) sub-micron-thick InGaAs photodiodes for future high-resolution image sensors. *Light Sci Appl* **13**, 311 (2024).
63. Zhang JS, Shao R, Xu HW et al. Flexible InGaAs/InAlAs avalanche photodiodes for short-wave infrared detection. *Nat Commun* **16**, 9367 (2025).
64. Wang Y, Gu Y, Cui AL et al. Fast uncooled mid-wavelength infrared photodetectors with heterostructures of van der Waals on epitaxial HgCdTe. *Adv Mater* **34**, 2107772 (2022).
65. Rogalski A. HgCdTe infrared detector material: history, status and outlook. *Rep Prog Phys* **68**, 2267–2336 (2005).
66. Zhang YJ, Ideue T, Onga M et al. Enhanced intrinsic photovoltaic effect in tungsten disulfide nanotubes. *Nature* **570**, 349–353 (2019).
67. Wang Z, Lu L, Meng JL et al. Emerging negative photoconductivity effect-based synaptic device for optoelectronic in-sensor computing. *Adv Mater* **37**, 2504710 (2025).
68. Iqbal MA, Liaqat A, Hussain S et al. Ultralow-transition-energy organic complex on graphene for high-performance shortwave infrared photodetection. *Adv Mater* **32**, 2002628 (2020).
69. Lu XW, Sun L, Jiang P et al. Progress of photodetectors based on the photothermoelectric effect. *Adv Mater* **31**, 1902044 (2019).
70. Basko D. A photothermoelectric effect in graphene. *Science* **334**, 610–611 (2011).
71. Ünlü MS, Strite S. Resonant cavity enhanced photonic devices. *J Appl Phys* **78**, 607–639 (1995).
72. Furchi M, Urich A, Pospischil A et al. Microcavity-integrated graphene photodetector. *Nano Lett* **12**, 2773–2777 (2012).
73. Sun HX, Li C, Li L et al. The development of customized perovskite photodetectors. *Nat Electron* **8**, 1170–1181 (2025).
74. Liu Y, Cheng R, Liao L et al. Plasmon resonance enhanced multicolour photodetection by graphene. *Nat Commun* **2**, 579 (2011).
75. Li ZY, Trendafilov S, Zhang FL et al. Broadband GaAsSb nanowire array photodetectors for filter-free multispectral imaging. *Nano Lett* **21**, 7388–7395 (2021).
76. Zhang FL, Zhang XT, Li ZY et al. A new strategy for selective area growth of highly uniform InGaAs/InP multiple quantum well nanowire arrays for optoelectronic device applications. *Adv Funct Mater* **32**, 2103057 (2022).
77. Mu G, Tan YM, Bi C et al. Visible to mid-wave infrared PbS/HgTe colloidal quantum dot imagers. *Nat Photonics* **18**, 1147–1154 (2024).
78. Ahn S, Shang JY, Patel SK et al. Intercalated graphene and

colloidal quantum dots for multispectral photodetection. *Adv Funct Mater* **34**, 2409523 (2024).
79. Kublitski J, Fischer A, Xing S et al. Enhancing sub-bandgap external quantum efficiency by photomultiplication for narrowband organic near-infrared photodetectors. *Nat Commun* **12**, 4259 (2021).
80. Konstantatos G, Sargent EH. Nanostructured materials for photon detection. *Nat Nanotechnol* **5**, 391–400 (2010).
81. Li X, Liu HY, Ke CM et al. Review of anisotropic 2D materials: controlled growth, optical anisotropy modulation, and photonic applications. *Laser Photonics Rev* **15**, 2100322 (2021).
82. Wang J, Jiang CZ, Li WQ et al. Anisotropic low-dimensional materials for polarization-sensitive photodetectors: from materials to devices. *Adv Opt Mater* **10**, 2102436 (2022).
83. Xia FN, Wang H, Jia YC. Rediscovering black phosphorus as an anisotropic layered material for optoelectronics and electronics. *Nat Commun* **5**, 4458 (2014).
84. Hu RJ, Lu XQ, Hao XT et al. An organic chiroptical detector favoring circularly polarized light detection from near-infrared to ultraviolet and magnetic-field-amplifying dissymmetry in detectivity. *Adv Mater* **35**, 2211935 (2023).
85. Chen CH, Yang ZH, Hang TY et al. Electrical-gain-assisted circularly polarized photodetection based on chiral plasmonic metamaterials. *Light Sci Appl* **14**, 265 (2025).
86. Zheng HQ, Wu ZQ, Shao J et al. High-performance circularly polarized light photodetector via temperature and high-energy photons modulation in 1D chiral perovskite single crystals. *Adv Funct Mater* e13402 (2025).
87. Wen YH, Chremmos I, Chen YJ et al. Spiral transformation for high-resolution and efficient sorting of optical vortex modes. *Phys Rev Lett* **120**, 193904 (2018).
88. Lei T, Zhang M, Li YR et al. Massive individual orbital angular momentum channels for multiplexing enabled by Dammann gratings. *Light Sci Appl* **4**, e257 (2015).
89. Zheng S, Wang J. Measuring orbital angular momentum (OAM) states of vortex beams with annular gratings. *Sci Rep* **7**, 40781 (2017).
90. Ji ZR, Liu WJ, Krylyuk S et al. Photocurrent detection of the orbital angular momentum of light. *Science* **368**, 763–767 (2020).
91. Lai JW, Ma JC, Fan ZP et al. Direct light orbital angular momentum detection in mid-infrared based on the type-II weyl semimetal $TaIrTe_4$. *Adv Mater* **34**, 2201229 (2022).
92. Yang DH, Lai JW, Fan ZP et al. Dimensionality-enhanced mid-infrared light vortex detection based on multilayer graphene. *Light Sci Appl* **14**, 116 (2025).
93. Mait JN, Euliss GW, Athale RA. Computational imaging. *Adv Opt Photonics* **10**, 409–483 (2018).
94. Wetzstein G, Ozcan A, Gigan S et al. Inference in artificial intelligence with deep optics and photonics. *Nature* **588**, 39–47 (2020).
95. Bao J, Bawendi MG. A colloidal quantum dot spectrometer. *Nature* **523**, 67–70 (2015).
96. Wang Z, Yi S, Chen A et al. Single-shot on-chip spectral sensors based on photonic crystal slabs. *Nat Commun* **10**, 1020 (2019).
97. Levoy M. Light fields and computational imaging. *Computer* **39**, 46–55 (2006).
98. Huang LL, Chen XZ, Mühlenbernd H et al. Three-dimensional optical holography using a plasmonic metasurface. *Nat Commun* **4**, 2808 (2013).
99. Redding B, Liew SF, Sarma R et al. Compact spectrometer based on a disordered photonic chip. *Nat Photonics* **7**, 746–751 (2013).
100. Yuan SF, Naveh D, Watanabe K et al. A wavelength-scale black phosphorus spectrometer. *Nat Photonics* **15**, 601–607 (2021).
101. Sherrott MC, Hon PWC, Fountaine KT et al. Experimental demonstration of >230° phase modulation in gate-tunable graphene-gold reconfigurable mid-infrared metasurfaces. *Nano Lett* **17**, 3027–3034 (2017).
102. Beeckman J. Liquid-crystal photonic applications. *Opt Eng* **50**, 081202 (2011).
103. Duarte MF, Davenport MA, Takhar D et al. Single-pixel imaging via compressive sampling. *IEEE Signal Process Mag* **25**, 83–91 (2008).
104. Miller DAB. Self-configuring universal linear optical component [Invited]. *Photonics Res* **1**, 1–15 (2013).
105. Candes EJ, Wakin MB. An introduction to compressive sampling. *IEEE Signal Process Mag* **25**, 21–30 (2008).
106. Molesky S, Lin Z, Piggott AY et al. Inverse design in nanophotonics. *Nat Photonics* **12**, 659–670 (2018).
107. Ma W, Liu ZC, Kudyshev ZA et al. Deep learning for the design of photonic structures. *Nat Photonics* **15**, 77–90 (2021).
108. Barbastathis G, Ozcan A, Situ GH. On the use of deep learning for computational imaging. *Optica* **6**, 921–943 (2019).
109. Hu JT, Liao K, Dinç NU et al. Subwavelength imaging using a solid-immersion diffractive optical processor. *eLight* **4**, 8 (2024).
110. Raissi M, Perdikaris P, Karniadakis GE. Physics-informed neural networks: a deep learning framework for solving forward and inverse problems involving nonlinear partial differential equations. *J Comput Phys* **378**, 686–707 (2019).
111. Cao ZX, Li N, Zhu LY et al. Aberration-robust monocular passive depth sensing using a meta-imaging camera. *Light Sci Appl* **13**, 236 (2024).
112. Wu J, Miao YC, Qi XR et al. Regulating energy band alignment for high-performance broadband perovskite photodetectors. *J Mater Chem A* **12**, 20425–20436 (2024).
113. Wu J, Luo DX, Wen PT et al. Engineering the polarization sensitivity in all-2D photodetectors composed of semimetal $MoTe_2$ and semiconductor WS_2. *Adv Opt Mater* **10**, 2201902 (2022).
114. Gao JB, Rao AM, Li HB et al. Carrier transport dynamics in high speed black phosphorus photodetectors. *ACS Photonics* **5**, 1412–1417 (2018).
115. Wu YC, Li DF, Wu CL et al. Electrostatic gating and intercalation in 2D materials. *Nat Rev Mater* **8**, 41–53 (2023).
116. Wang FK, Zhu S, Chen WD et al. Bipolar-barrier tunnel heterostructures for high-sensitivity mid-wave infrared photodetection. *Light Sci Appl* **14**, 246 (2025).
117. Chen YF, Wang Y, Wang Z et al. Unipolar barrier photodetectors based on van der Waals heterostructures. *Nat Electron* **4**, 357–363 (2021).
118. Zhang YR, Yang EB, Yoon HH et al. Reconstructive spectrometers: hardware miniaturization and computational reconstruction. *eLight* **5**, 23 (2025).
119. Yoon HH, Fernandez HA, Nigmatulin F et al. Miniaturized spectrometers with a tunable van der Waals junction. *Science* **378**, 296–299 (2022).
120. Yuan HT, Liu XG, Afshinmanesh F et al. Polarization-sensitive broadband photodetector using a black phosphorus vertical *p-n* junction. *Nat Nanotechnol* **10**, 707–713 (2015).
121. Tong L, Huang XY, Wang P et al. Stable mid-infrared polarization imaging based on quasi-2D tellurium at room temperature. *Nat*

Commun **11**, 2308 (2020).
122. He KX, Ran WH, Xu SD et al. Polarization signal amplification of 2D GeSe-based polarization-sensitive photodetectors. *Adv Mater* **37**, 2509066 (2025).
123. Liu MX, Qi LJ, Zou YT et al. Uncooled near- to long-wave-infrared polarization-sensitive photodetectors based on $MoSe_2/PdSe_2$ van der Waals heterostructures. *Nat Commun* **16**, 2774 (2025).
124. Chen C, Gao L, Gao WR et al. Circularly polarized light detection using chiral hybrid perovskite. *Nat Commun* **10**, 1927 (2019).
125. Gu QF, Zha JJ, Chen CL et al. Constructing chiral covalent-organic frameworks for circularly polarized light detection. *Adv Mater* **36**, 2306414 (2024).
126. Xiong YF, Wang YS, Zhu RZ et al. Twisted black phosphorus-based van der Waals stacks for fiber-integrated polarimeters. *Sci Adv* **8**, eabo0375 (2022).
127. Deng WJ, Dai MJ, Wang CW et al. Switchable unipolar-barrier van der Waals heterostructures with natural anisotropy for full linear polarimetry detection. *Adv Mater* **34**, 2203766 (2022).
128. Ma XF, Wang ZP, Qin QG et al. Simultaneous AoLP and DoLP detection in a bias-switchable $PdSe_2/MoS_2/PdSe_2$ heterojunction for polarization discrimination. *Adv Mater* **37**, 2500572 (2025).
129. Fang C, Li JZ, Zhou BX et al. Self-powered filterless on-chip full-Stokes polarimeter. *Nano Lett* **21**, 6156–6162 (2021).
130. Ge MW, Yao Y, Wang T et al. Accurate single-shot full-Stokes detection enabled by heterogeneous grain orientations in polycrystalline films. *Nat Commun* **16**, 5603 (2025).
131. Zhang SK, Jiao HX, Chen Y et al. Multi-dimensional optical information acquisition based on a misaligned unipolar barrier photodetector. *Nat Commun* **15**, 7071 (2024).
132. Tang HN, Lou BC, Du F et al. An adaptive moiré sensor for spectro-polarimetric hyperimaging. *Nat Photonics* **19**, 463–470 (2025).
133. Ma C, Yuan SF, Cheung P et al. Intelligent infrared sensing enabled by tunable moiré quantum geometry. *Nature* **604**, 266–272 (2022).
134. Wang FK, Zhu S, Chen WD et al. Multidimensional detection enabled by twisted black arsenic-phosphorus homojunctions. *Nat Nanotechnol* **19**, 455–462 (2024).
135. Guo LQ, Sun HX, Wang M et al. Polarization and spectrum multi-dimensional sensitive perovskite photodetectors. *Adv Opt Mater* **12**, 2301998 (2024).
136. Iwanaga M. Photonic metamaterials: a new class of materials for manipulating light waves. *Sci Technol Adv Mater* **13**, 053002 (2012).
137. Hao JM, Qiu M, Zhou L. Manipulate light polarizations with metamaterials: from microwave to visible. *Front Phys China* **5**, 291–307 (2010).
138. Oliveri G, Werner DH, Massa A. Reconfigurable electromagnetics through metamaterials-a review. *Proc IEEE* **103**, 1034–1056 (2015).
139. Zheng ZP, Huang YJ, Wu F et al. Multidimensional modulation of light fields via a combination of two-dimensional materials and meta-structures. *Sci China Inf Sci* **66**, 160403 (2023).
140. Shi JH, Li ZJ, Sang DK et al. THz photonics in two dimensional materials and metamaterials: properties, devices and prospects. *J Mater Chem C* **6**, 1291–1306 (2018).
141. Dai ZG, Hu GW, Ou QD et al. Artificial metaphotonics born naturally in two dimensions. *Chem Rev* **120**, 6197–6246 (2020).
142. Jiang H, Fu JT, Wei JX et al. Synergistic-potential engineering enables high-efficiency graphene photodetectors for near- to mid-infrared light. *Nat Commun* **15**, 1225 (2024).
143. Wu JF, Zhang JL, Jiang RQ et al. High-sensitivity, high-speed, broadband mid-infrared photodetector enabled by a van der Waals heterostructure with a vertical transport channel. *Nat Commun* **16**, 564 (2025).
144. Dai MJ, Wang CW, Qiang B et al. Long-wave infrared photothermoelectric detectors with ultrahigh polarization sensitivity. *Nat Commun* **14**, 3421 (2023).
145. Li W, Coppens ZJ, Besteiro LV et al. Circularly polarized light detection with hot electrons in chiral plasmonic metamaterials. *Nat Commun* **6**, 8379 (2015).
146. Wei JX, Chen Y, Li Y et al. Geometric filterless photodetectors for mid-infrared spin light. *Nat Photonics* **17**, 171–178 (2023).
147. Zhang GY, Lyu XY, Qin YL et al. High discrimination ratio, broadband circularly polarized light photodetector using dielectric achiral nanostructures. *Light Sci Appl* **13**, 275 (2024).
148. He CL, Tang ZL, Wang CH et al. Gradient-metasurface-contact photodetector for visible-to-near-infrared spin light. *Adv Mater* **37**, 2418405 (2025).
149. Guo C, Yu JY, Deng SK. Hybrid metasurfaces of plasmonic lattices and 2D materials. *Adv Funct Mater* **33**, 2302265 (2023).
150. Deng ZL, Li GX. Metasurface optical holography. *Mater Today Phys* **3**, 16–32 (2017).
151. Meinzer N, Barnes WL, Hooper IR. Plasmonic meta-atoms and metasurfaces. *Nat Photonics* **8**, 889–898 (2014).
152. Chen J, Hu SS, Zhu SN et al. Metamaterials: from fundamental physics to intelligent design. *Interdiscip Mater* **2**, 5–29 (2023).
153. Li J, Lu XG, Li H et al. Racemic dielectric metasurfaces for arbitrary terahertz polarization rotation and wavefront manipulation. *Opto-Electron Adv* **7**, 240075 (2024).
154. Guo YH, Pu MB, Zhang F et al. Classical and generalized geometric phase in electromagnetic metasurfaces. *Photonics Insights* **1**, R03 (2022).
155. Guo YH, Zhang SC, Pu MB et al. Spin-decoupled metasurface for simultaneous detection of spin and orbital angular momenta via momentum transformation. *Light Sci Appl* **10**, 63 (2021).
156. Wei JX, Li Y, Wang L et al. Zero-bias mid-infrared graphene photodetectors with bulk photoresponse and calibration-free polarization detection. *Nat Commun* **11**, 6404 (2020).
157. Wang CH, He CL, Liu L et al. Rotation-symmetry grating contact photodetector for visible full linear polarimetry detection. *Nano Lett* **25**, 5794–5802 (2025).
158. Wei JX, Xu C, Dong BW et al. Mid-infrared semimetal polarization detectors with configurable polarity transition. *Nat Photonics* **15**, 614–621 (2021).
159. Li RZ, Zhang XL, Zhong F et al. On-chip metasurface-mediated $MoTe_2$ photodetector with electrically tunable polarization-sensitivity. *Adv Opt Mater* **13**, 2402668 (2025).
160. Li LF, Wang JZ, Kang L et al. Monolithic full-stokes near-infrared polarimetry with chiral plasmonic metasurface integrated graphene-silicon photodetector. *ACS Nano* **14**, 16634–16642 (2020).
161. Dai MJ, Wang CW, Qiang B et al. On-chip mid-infrared photothermoelectric detectors for full-Stokes detection. *Nat Commun* **13**, 4560 (2022).
162. Deng J, Shi MD, Liu XS et al. An on-chip full-Stokes polarimeter based on optoelectronic polarization eigenvectors. *Nat Electron* **7**, 1004–1014 (2024).
163. Liu XS, Chen YZ, Kong XH et al. Metaphotonic photodetectors for

direct Stokes quantification. *Nat Electron* **8**, 1099–1107 (2025).
164. Chen M, Wang YX, Zhao ZR. Monolithic metamaterial-integrated graphene terahertz photodetector with wavelength and polarization selectivity. *ACS Nano* **16**, 17263–17273 (2022).
165. Xie JS, Ren ZH, Wei JX et al. Zero-bias long-wave infrared nanoantenna-mediated graphene photodetector for polarimetric and spectroscopic sensing. *Adv Opt Mater* **11**, 2202867 (2023).
166. Chu YT, Chen PL, Huang SH et al. All-van-der-Waals heterostructure of MoS_2 grating and InSe flake for spectrally selective polarization-sensitive photodetection in NIR region. *ACS Nano* **19**, 18545–18555 (2025).
167. Jiang H, Chen YZ, Guo WY et al. Metasurface-enabled broadband multidimensional photodetectors. *Nat Commun* **15**, 8347 (2024).
168. Wen S, Xue XY, Wang S et al. Metasurface array for single-shot spectroscopic ellipsometry. *Light Sci Appl* **13**, 88 (2024).
169. He HY, Lai FX, Zhang Y et al. Spectro-polarimetric detection enabled by multidimensional metasurface with quasi-bound states in the continuum. *Opto-Electron Adv* **8**, 250015 (2025).
170. Cai GY, Li YH, Zhang Y et al. Compact angle-resolved metasurface spectrometer. *Nat Mater* **23**, 71–78 (2024).
171. Fan YD, Huang WA, Zhu F et al. Dispersion-assisted high-dimensional photodetector. *Nature* **630**, 77–83 (2024).
172. Dai MJ, Wang CW, Sun FY et al. On-chip photodetection of angular momentums of vortex structured light. *Nat Commun* **15**, 5396 (2024).
173. Zhang ZK, Zhang T, Zhang ZP et al. Deep learning-enabled ultra-broadband terahertz high-dimensional photodetector. *Nat Commun* **16**, 8133 (2025).
174. Akinwande D, Huyghebaert C, Wang CH et al. Graphene and two-dimensional materials for silicon technology. *Nature* **573**, 507–518 (2019).
175. Siew SY, Li B, Gao F et al. Review of silicon photonics technology and platform development. *J Lightwave Technol* **39**, 4374–4389 (2021).
176. Chen X, Milosevic MM, Stanković S et al. The emergence of silicon photonics as a flexible technology platform. *Proc IEEE* **106**, 2101–2116 (2018).
177. Meglinski I, Lopushenko I, Sdobnov A et al. Phase preservation of orbital angular momentum of light in multiple scattering environment. *Light Sci Appl* **13**, 214 (2024).
178. Rota MB, Krieger TM, Buchinger Q et al. A source of entangled photons based on a cavity-enhanced and strain-tuned GaAs quantum dot. *eLight* **4**, 13 (2024).
179. Piggott AY, Lu J, Lagoudakis KG et al. Inverse design and demonstration of a compact and broadband on-chip wavelength demultiplexer. *Nat Photonics* **9**, 374–377 (2015).
180. Bütow J, Sharma V, Brandmüller D et al. Photonic integrated processor for structured light detection and distinction. *Commun Phys* **6**, 369 (2023).
181. Liu XM, Zhang ZX, Zhou JK et al. Development of photonic in-sensor computing based on a mid-infrared silicon waveguide platform. *ACS Nano* **18**, 22938–22948 (2024).
182. Zhu SK, Zheng ZH, Meng WJ et al. Harnessing disordered photonics via multi-task learning towards intelligent four-dimensional light field sensors. *PhotoniX* **4**, 26 (2023).
183. Gu ZJ, Zhang WL, Yu Y et al. Disordered-guiding photonic chip enabled high-dimensional light field detection. *Nat Commun* **16**, 7741 (2025).
184. Gu ZJ, Shi Y, Zhu ZM et al. All-integrated multidimensional optical sensing with a photonic neuromorphic processor. *Sci Adv* **11**, eadu7277 (2025).

Acknowledgements

The authors acknowledge financial support from the National Key R&D Program of China (2022YFA1204300), National Natural Science Foundation of China (52221001, 62090035 and 62175061), the Open Project Program of Key Laboratory of Nanodevices and Applications, and Suzhou Institute of Nano-Tech and Nano-Bionics, Chinese Academy of Sciences (22ZS01).

Author contributions

The manuscript was written through the contributions of all authors. All authors have given approval to the final version of the manuscript.

Competing interests

The authors declare no competing financial interests.

Published by Editorial Office of *Opto-Electronic Technology*, Institute of Optics and Electronics, Chinese Academy of Sciences.